

Structural Analysis of Biological
Membranes and Proteins by Atomic
Force Microscopy

Vom Fachbereich Biologie der Universität Hannover

zur Erlangung des Grades

Doktor der Naturwissenschaften

Dr. rer. nat.

genehmigte Dissertation

von

Dipl. Phys. Oliver Enders

geboren am 27. März 1972 in Wildeshausen

2004

Referent: Prof. Dr. Hans-Albert Kolb
Korreferent: Prof. Dr. Wolfgang Ertmer
Tag der Promotion: 6. Mai 2004

Contents

1	Kurzdarstellung	9
2	Abstract	13
3	Introduction and content	17
	References	27
4	Morphology of Native and Reconstituted Biological Membranes and their Components Analysed by Atomic Force Microscopy	29
	Abstract	30
4.1	Introduction	30
4.2	Results and discussion	32
4.2.1	Images of the living peritoneal macrophage . . .	32
4.2.2	Force curves on peritoneal macrophages	36
4.2.3	Reconstituted mica-supported phospholipid bi- layers	39
4.2.4	Nicotinic acetylcholine receptor complex	43
4.2.5	Interfaces of the vacuolar membrane	47
4.3	Conclusion	50
	References	53
5	Identification of Membrane Proteins Imaged by Atomic Force Microscopy Using a Template Matching Algorithm	63

6	Analysis of Protein Crystal Growth at Molecular Resolution by Atomic Force Microscopy	65
	Abstract	66
6.1	Introduction	67
6.2	Materials and methods	68
	6.2.1 Sample preparation	68
	6.2.2 Atomic force microscopy	68
6.3	Results	70
	6.3.1 Size and kinetics of growth steps of the (110) crystal face	70
	6.3.2 Linescan of (101) surface at molecular resolution	75
6.4	Discussion	78
6.5	Conclusion	80
	References	83
7	Structural Calorimetry of Main Transition of Supported DMPC Bilayers by Temperature Controlled AFM	87
	Abstract	88
7.1	Introduction	88
7.2	Material and Methods	91
	7.2.1 Sample preparation	91
	7.2.2 Temperature controlled atomic force microscope	92
	7.2.3 Image acquisition and processing	93
7.3	Results	94
	7.3.1 Topography of supported DMPC bilayers in the fluid-crystalline- and gel-phase	94
	7.3.2 Topography at temperatures of main transition	96
	7.3.3 Structural calorimetry of main transition by image analysis	98

7.3.4	Phase transition of DMPC bilayer in the presence of heptanol or Ca^{2+}	101
7.3.5	Cooperative unit n_c	104
7.4	Discussion	106
7.4.1	Structural properties of ripple phase	107
7.4.2	Structure of the bilayer at main transition	107
7.4.3	Structural calorimetry and estimation of the cooperative unit n_c	108
7.4.4	Effect of heptanol and Ca^{2+} on main transition	110
7.4.5	Dependence of ΔH on T_0	111
7.5	Acknowledgment	112
	References	115
8	Lorentz-force-induced Excitation of Cantilevers for Oscillation-Mode Scanning Probe Microscopy	125
	Abstract	126
8.1	Introduction	126
8.2	Material and methods	128
8.2.1	Basic setup	128
8.2.2	Micro-structuring the cantilever chip	131
8.3	Results	134
8.4	Conclusion	139
8.4.1	Thermal and Lorentz force induced excitation	140
	References	143
	Acknowledgment	147
	Curriculum vitae	149

List of Figures

3.1	Working principle of atomic force microscopy	17
4.1	Living murine peritoneal macrophage	33
4.2	Macrophage particle phagocytosis	35
4.3	Force curves at macrophages	37
4.4	Mica supported phospholipid bilayers	40
4.5	IgG-doped phospholipid bilayer	41
4.6	<i>Xenopus laevis</i> oocyte membrane patches	44
4.7	Nicotinic acetylcholine-receptor (nAChR)	45
4.8	Vacuolar membrane of barley leaves	48
6.1	(110)-surface of lysozyme crystal	71
6.2	Real time observation of the growth of (110)-surface	72
6.3	Nucleation on (110)-surface	72
6.4	Molecular resolved (110)-surface	73
6.5	(101)-surface at high resolution	76
6.6	Linescan images of a growing edge	77
7.1	Supported DMPC bilayer in L_{α} -phase and $P_{\beta'}$ -phase	95
7.2	Bilayer at decreasing temperatures	97
7.3	Post-processing of a supported DMPC bilayer image	99
7.4	Fraction of $P_{\beta'}$ -phase as function of T	100

7.5	DMPC bilayer at increasing heptanol or Ca^{2+} concentrations	103
7.6	Determination of n_c	105
7.7	T_0 dependence of transition enthalpy	113
8.1	Schematic setup for Lorentz force excitation of the cantilever	129
8.2	Power spectrum of a Lorentz force excited cantilever in air	132
8.3	Power spectrum of a Lorentz force excited cantilever placed in water	133
8.4	Amplitude spectrum and power spectrum of cantilever oscillation which is excited by Lorentz force superimposed by a thermal induced oscillation	137

1 Kurzdarstellung

Die Erfindung des Rasterkraftmikroskops 1986 von Binnig, Quate und Gerber gewährt Biowissenschaftlern Einblick in die molekulare Welt mit einer Auflösung, die sonst nur mit der Elektronenmikroskopie erreichbar ist. Jedoch bietet das Rasterkraftmikroskop den entscheidenden Vorteil, Proben unter kontrollierten physiologischen Inkubationsbedingungen in Echtzeit abbilden zu können; biologische Strukturen können somit *in situ* untersucht werden.

Die vorliegende Dissertationsschrift besteht aus fünf am Institut für Biophysik der Universität Hannover durchgeführten wissenschaftlichen Arbeiten zum Thema der Rasterkraftmikroskopie biologischer Objekte. Vorrangiges Ziel der Arbeit ist die Darstellung der Struktur biologischer Membranen mit molekularer Auflösung. Die Bandbreite der untersuchten Systeme reicht von lebenden peritonealen Makrophagen über isolierte native Plasmamembranen und Tonoplasten, bis hin zur Darstellung einzelner Antikörpermoleküle, die an rekonstituierten und dotierten künstlichen Membranen gebunden werden [1].

Da die laterale Auflösung der topographischen Darstellung lebender Zellen aufgrund ihrer Weichheit begrenzt ist, ist die Untersuchung isolierter und zytoskelettfreier, nativer Membranen, wie der vakuolären Membran, notwendig. Eingehende Untersuchungen am Tonoplast der Mesophyllzelle aus *Hordeum vulgare* L. illustrieren die Heterogenität der Struktur nativer Membranen, die die eindeutige Identifikation einzelner Membranmoleküle erschwert [2]. Am Beispiel der H^+ -ATPase

wird die Identifikation von Membranproteinen mit bildverarbeitenden Methoden unter Zuhilfenahme bekannter geometrischer Daten gezeigt.

Da die Strukturaufklärung von Proteinen deren Kristallisation voraussetzt, wird das Rasterkraftmikroskop eingesetzt, um das Wachstum von Proteinkristallen zu analysieren [3]. Mittels aufeinanderfolgenden Aufnahmen wird das Wachstum tetragonaler Lysozymkristalle zeitnah und mit molekularer Auflösung räumlich dargestellt und in der Kinetik analysiert. Zur Analyse der Wachstumskinetik konnte die Zeitauflösung mittels der *linescan* Methode weiter verbessert werden. Die Ergebnisse liefern die Voraussetzung für eine mögliche rasterkraftmikroskopisch gesteuerte Induktion der Keime einzelner Proteinkristalle¹.

Neben der Struktur vieler Membranproteine sind gegenwärtig Fragen zu strukturellen Veränderungen der Lipiddoppelschicht unter Berücksichtigung des Phasenverhaltens und dessen Auswirkung auf die Funktion der Membranproteine noch weitgehend ungeklärt. Am Beispiel von Glimmer-unterstützten, planaren Dimyristoylphosphatidylcholin-Lipiddoppelschichten wird der Übergang aus der flüssig-kristallinen L_α - in die Gel- oder $P_{\beta'}$ -Phase untersucht [4]. Hierzu war die Neuentwicklung einer Temperaturregelung für das Rasterkraftmikroskop erforderlich. Die $P_{\beta'}$ -Phase bildet sich nach der van't Hoff'schen Temperaturabhängigkeit aus der flüssig-kristallinen L_α -Phase und ist durch eine charakteristische Rippelstruktur gekennzeichnet. Die Abhängigkeit der Phasenübergangstemperatur und der Übergangsenthalpie der Lipiddoppelschichten von den Modulatoren Heptanol und Ca^{2+} kann mittels Bildanalyse bestimmt werden. Es

¹Wiechmann, Leisten, Enders, Kolb: in Vorbereitung

ergibt sich eine lineare Abhängigkeit der Übergangsenthalpie von der Phasenübergangstemperatur, die auf eine Differenz der Wärmekapazität zwischen den beiden Phasen zurückgeführt werden kann. Erstmals wird in dieser Arbeit die kooperative Einheit von Lipidmolekülen aus strukturellen Daten ermittelt. Diese Einheit beschreibt das kollektive Verhalten von Lipidmolekülen während des Phasenübergangs.

Einen wesentlichen Beitrag zur Vergrößerung der Auflösung in der Abbildung von vergleichsweise weichen biologischen Proben liefert der oszillatorische Messmodus, der so genannte *Tapping-Modus*. Eine weitere Verbesserung besteht in der Entwicklung einer elektromagnetischen Methode zur direkten Schwingungsanregung der rasterkraftmikroskopischen Sonde [5]. Diese Methode nutzt die Wirkung der Lorentzkraft auf einen stromdurchflossenen Kantilever in einem statischen Magnetfeld. Im Gegensatz zu der bisher gebräuchlichen Anregung der Messsonde mittels einer piezomechanisch erzeugten Vibration der Messzelle kann mit der auf Lorentzkraft basierenden Methode eine unerwünschte Schwingung des Probenträgers und der Probe weitgehend unterdrückt werden.

Mit der neu entwickelten Temperatursteuerung und der verbesserten Auflösung durch die elektromagnetische Anregungsform kann auf der Basis der identifizierten und charakterisierten Membrankomponenten die Dynamik von Protein-Lipidwechselwirkungen in den so genannten *Lipid Rafts* unter quasi Echtzeitbedingungen molekular aufgeklärt werden. Diese Untersuchungen wurden bereits begonnen und können einen wesentlichen Beitrag zum Verständnis der Struktur-Funktionsbeziehung der Lipid Rafts leisten.

Schlagworte: Rasterkraftmikroskopie, biologische Membranen, Lipide

2 Abstract

The invention of the atomic force microscope by Binnig, Quate and Gerber in 1986 allows life-scientists the exploration of the molecular world with a resolution, which can otherwise be achieved by electron microscopic methods only. However, the atomic force microscope has the major advantage to image samples in fluid environment and at real time. Hence, biological structures can be analyzed *in situ* and at physiological conditions.

The present dissertation is based on five publications on the research which has been conducted at the Institute of Biophysics, University of Hannover in the field of atomic force microscopy of biological samples. The presented experiments and results are focused to the representation of the structure of biological membranes at molecular resolution. The bandwidth of objects which are analyzed ranges from living peritoneal macrophages, isolated native plasma membranes and tonoplasts to single antibodies, which are bound to reconstituted and appropriately doped artificial membranes [1].

The lateral resolution of topographies of living cells is limited, which is caused by their softness. This motivated a detailed elucidation of the native vacuolar membrane (tonoplast) of the mesophyll cell of *Hordeum vulgare* L.. Tonoplasts are free of cytoskeleton and can be imaged at high resolution [2]. The results illustrate the heterogeneity in the surface structure of native membranes, which hinders the unique identification of single membrane molecules. However, the specific

identification of membrane proteins by image processing methods is exemplary demonstrated in the case of H^+ -ATPase.

The atomic resolution of proteins requires the availability of pure and sufficient large protein crystals. For extending the understanding of the growth process of protein crystals, the capability of the atomic force microscope to achieve molecular resolution imaging of samples at controlled environment is exploited to monitor protein crystal growth [3]. The growing of tetragonal protein crystals from lysozyme is recorded in real time and the kinetics are analyzed. By application of the linescan mode, the time resolution is further improved in order to analyze the kinetics of crystal growth. The results present the basis for a possible induction of nuclei for the growth of single protein crystals by atomic force microscopy¹.

Apart from the dynamics of the structure of membrane proteins, questions concerning structural changes and the phase properties of lipid bilayers and their effects on the function of membrane proteins are still not fully understood. The phase transition of an artificial membrane from fluid-crystalline (L_{α^-}) to the gel- or $P_{\beta'}$ -phase is elucidated by the example of mica supported bilayers of dimyristoylphosphatidylcholine [4]. For this, the atomic force microscope is equipped with a temperature control. The $P_{\beta'}$ -phase emerges from the L_{α^-} -phase following a van't Hoff temperature like dependence, and is characterized by a distinguishing ripple structure. The dependence of the phase transition temperature and enthalpy on heptanol concentration and the presence of Ca^{2+} is determined using image analysis. From this a linear dependence of the transition enthalpy on the phase transition temperature is obtained and discussed in terms of a difference

¹Wiechmann, Leisten, Enders, Kolb: in preparation

in heat capacity of the L_α - and $P_{\beta'}$ -phase. For the first time, the cooperative unit describing the collective behavior of the lipid molecules at phase transition is determined from structural data.

A substantial contribution to improve the resolution of soft biological samples presents the oscillation mode, which is also called *tapping mode*. A further improvement of this mode is represented by the implementation of an electromagnetic method to excite the oscillation of the atomic force sensor [5]. The method is based on the effect of the Lorentz force on the cantilever, which is induced by an electrical current in the reflection layer placed in a static magnetic field. Unlike the conventional mechanical excitation of the atomic force sensor by a piezomechanically induced vibration of the measurement chamber, a resolution-limiting vibration of the sample-stage and the sample may be significantly reduced by the Lorentz force based excitation.

By the newly developed temperature control and by the advanced Lorentz force based excitation method, the dynamics of the interaction between lipids and proteins in the so called *lipid rafts* may be elucidated at molecular resolution and in real time. Atomic force microscopic studies have been started and may provide a significant contribution to the understanding of the structure/function relationship of lipid rafts.

Key words: Scanning Force Microscopy, biological membranes, lipids

3 Introduction and content

One of the most important driving forces for the progress in life science is the extension of the limits of the visible. This can be impressively illustrated by the work of Hooke in 1665 who developed the concept of the *cell* in biological tissue by the use of microscopes, which enabled him to see and to identify structures which had never been observed before.

Nowadays the advances in physics and technology allow to routinely resolve biological structures at molecular level. Occasionally, even atomic details are revealed by the use of synchrotron radiation supported x-ray diffraction analysis, if the creation of sufficiently large and pure macromolecular crystals was successful.

One exceptional method was invented by Binnig, Quate and Gerber, who developed the *atomic force microscope* on the basis of the noble prize¹ honored method of scanning tunneling microscopy in 1986. The principle of an atomic force microscope can be described by an atomically sharp tip, which is attached to a cantilever and

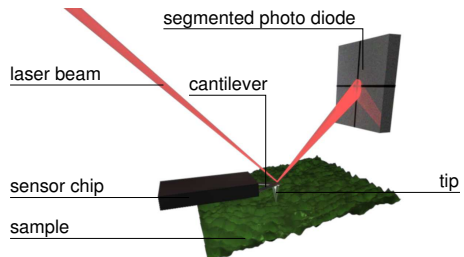


Figure 3.1: Illustration of the working principle of atomic force microscopy.

¹Binnig and Rohrer, 1986

scanned line by line across a sample by piezomechanical devices. A laser beam, which is focused to the backside of the cantilever, helps to read out the deflection of the cantilever by irradiating a segmented and therefore position sensitive photo-diode. The vertical position of the tip can be measured with sub-nanometer accuracy. Since the vertical deflection of the cantilever is related to the force between tip and sample by the spring constant of the cantilever, the force can be held constant by an electronic feedback circuit. In this way, the topology of the sample surface can be recorded and the resolution may be sufficient to image even single atoms.

Especially in life science, the atomic force microscope helps to explore the molecular world with a resolution which has otherwise only been achieved by electron microscopic techniques. It is shown, that atomic force microscopy provides the unique approach for the analysis of biological samples at conditions close to the physiological situation. The resolution can be continuously tuned over a range of four orders of magnitude. This allows to investigate objects ranging from the level of living cells with dimensions of several tens of micrometer to single proteins attached to reconstituted membranes with dimensions of only a few nanometer [1]. Having these unique properties of atomic force microscopy in mind, the question arises whether it is possible to observe the structure and dynamics of cell membranes as well as the membrane proteins in their native environment at molecular resolution.

To realize the concept of imaging living cells while retaining physiological conditions, peritoneal macrophages were isolated from mouse and imaged in physiological phosphate buffered solution [1]. Macrophages have the tendency to phagocytose non-self objects like la-

tex beads. It was thus possible to show that these cells stay alive during the imaging process by monitoring the locomotion of the cells and the process of phagocytosis. Additionally it could be demonstrated, that the macrophages show an active response to the imaging tip resulting in an induced elevation of the central region of the cell as if the macrophage tries to phagocytose the tip. However, on the nanometer length scale, individual molecules were not resolved. The limited resolution is most probably caused by the softness of living cells. The intracellular cytoskeleton which supports the plasma membrane is flexible and changeable, whereby the sample can be pushed aside by the scanning tip. The force distance curves on living cells revealed an extraordinary small Young modulus. The corresponding effective spring constant is one to two orders of magnitude smaller than the spring constant of the cantilever of the force sensor. As a consequence the sample is strongly deformed by the scanning tip leading to an increased contact area which reduces the achievable resolution significantly.

On the other hand, a supported artificial membrane which was made from a suspension of vesicles composed of a mixture of synthetic phospholipids with a small amount of a lipid with Texasred-phosphatidylamine head group could be imaged at nanometer resolution on a muscovite mica support [1]. In this case, single antibody molecules, which were bound to the Texasred labels could be clearly resolved. The improved resolution is most probably caused by the low thickness of the bilayer in the order of only 5 nm formed on a rigid support. If the loading force of the tip is sufficiently low, the membrane is only indented insignificantly leading to a sufficient resolution to display individual proteins. These promising initial measurements

already pointed out, that the achievable lateral resolution depends on the simplicity, purity and hardness of the analyzed sample.

For the further experiments a native biological membrane is chosen, which has similar mechanical properties as artificial bilayers. Therefore the membrane of the vacuole, the so called *tonoplast* was selected for further experiments [2]. Vacuoles can be retained functionally intact throughout the isolation procedure. They resemble unilamellar giant liposomes, they do not contain any cytoskeleton and therefore can be spread and firmly attached to the sample support in similar way as artificial lipid bilayers. Vacuoles were isolated from mesophyll cells of *Hordeum vulgare* L. and adsorbed to a support made of muscovite mica. The adsorption process induced a rupture of the vacuole which allowed to image the cytoplasmatic as well as the intravacuolar surface of flat patches of the tonoplast with a significantly improved resolution compared to the system of living cells in physiological solution. The tonoplast consists of a large variety of integral proteins and lipids, where the H^+ -ATPase is the most abundant membrane protein and was therefore the topic of further study. Its characteristic cytoplasmatic head and stalk structure (V_1) had been elucidated in detail by electron microscopy and x-ray diffraction methods. From these data and taking the tip geometry into account, a geometrical model was derived, which allowed to simulate the topography of the cytoplasmatic V_1 -part of the molecule. By newly developed image processing methods the simulated topography was used as a template to identify the H^+ -ATPase within the recorded topographies. The dimension of the cytoplasmatic region of the molecule was found to be in suitable agreement with published data. It thus may be possible to acquire real time structural data from individual active H^+ -ATPase

molecules *in situ* providing a deeper understanding of the adenosine-triphosphate hydrolyzing reaction cycle.

Although the resolution could be improved by the use of the tonoplast, submolecular resolution was not achieved in the case of native membranes. This may be explained by tip contamination and lateral mobility of the membrane components to be imaged.

In order to improve the resolution further and to observe structural data of proteins in real time in controlled fluid environment, the formation of tetragonal lysozyme crystals was analyzed [3]. It is well known, that due to the possibility to apply averaging procedures to topographies of proteins in crystalline arrangement yields a lateral resolution significantly higher than for images of individual disordered molecules of low density. Furthermore, the neighboring proteins form a mechanical support of the imaged protein reducing lateral movement and supporting the virtual rigidity of the protein which interacts with the tip of the force sensor. In addition, there is no general method known to identify the type and nature of single membrane proteins within their native environment.

Lysozyme and its crystallization properties are well characterized and the protein is available in large amounts at high purification. Therefore it is often chosen as a model system to elucidate general aspects of protein crystallization. The (101) as well as (110) face of fully hydrated crystals which were grown on mica could be resolved showing the corresponding unit cells with molecular detail. Appropriate control of the imaging buffer allowed the crystals to grow during the imaging process layer by layer. Growing crystal faces and 2D-nucleation events could be observed by recording series of consecutive images in real time. From these sequences the velocity of steps representing the boundaries of growing protein layers were determined quantitatively.

For the understanding of the dynamics of protein crystal growth it is important to know whether protein crystals grow by attachment of single molecules to the boundaries of crystal faces or if preaggregates with a larger number of molecules are formed in solution which then attach to the crystal surface in a single growth step. By using the linescan method, the time resolution could be improved by about two orders of magnitude corresponding to the time scale of single growth steps. From structural data it was concluded that preaggregates of about 10 tetramers are formed in solution, which then attach to the crystal within a time scale of about 80 ms.

It is known that the function of membrane proteins can depend on the specific lipid composition of the bilayer at the local environment of the protein. Bilayers with physiological lipid composition generally are in fluid phase, where the lipid molecules can individually diffuse within the membrane plane. However more recently the existence of phase separated lipid domains was proposed, which are characterized by an increased content of sphingolipids which lead to a higher ordered gel phase. This leads to reduced mobility of the lipids and proteins. It is proposed that these lipid domains, which are called *lipid rafts*, are responsible for a lipid mediated regulation of a number of membrane proteins and are involved in infection processes. Agents like alcohols or anesthetics have the potential to alter the thermodynamic properties of the lipids by interacting with their hydrophobic acyl chains. As example it is possible to inhibit gap-junctional coupling of neighboring cells by extracellular application of the long chain alcohol heptanol. The question arises, whether this regulation can be caused by a change of thermodynamic properties of lipid rafts, which embed the cell-to-cell channels of the gap junction. This heptanol induced gating of cell-to-cell channels is proposed to be correlated to a change

in the surface structure and fluidity of the bilayer. In order to study the influence of heptanol on the structure and the thermodynamic parameters of the main phase transition - phase transition temperature and transition enthalpy -, mica supported bilayers of dimyristoylphosphatidylcholine were chosen as a model system. This specific lipid has the advantage of a main transition temperature between fluid- (L_{α} -) and gel- ($P_{\beta'}$ -) phase close to room temperature. It can be imaged at a resolution in the order of 0.1 nm in z- and 1 to 10 nm in lateral direction [4]. For these experiments a temperature controlled atomic force microscope was developed with an accuracy in the order of 0.1 K. The temperature in the fluid cell had to be stabilized to reduce thermal drifts of the cantilever by bending. In addition, vibrations induced by the cooling devices had to be minimized to retain a height resolution in the sub-nanometer range. From image sequences of the surface of the supported bilayer in dependence of the sample temperature, thermodynamic characteristics could be extracted by image processing, which are usually determined by differential scanning calorimetry. Simultaneous recording of detailed structural data provided new insights to the formation of the $P_{\beta'}$ -phase, which is characterized by distinguishing surface undulations of the membranes, called *ripples*. For the first time, evidence was obtained for the existence of cooperative units from structural data, which as yet had been postulated to explain the discrepancy of calorimetric and van't Hoff transition enthalpies determined by differential scanning calorimetry. The cooperative unit was found to be organized as small interconnected domains of lipid molecules, which change their phase state in a collective process. Analyzing the effect of the gap junction regulating agents heptanol and Ca^{2+} , it was found that the temperature of the main phase transition is decreased by heptanol and increased by Ca^{2+} . It

turned out, that the transition enthalpy depends linearly on the temperature of the main phase transition in the observed temperature range. It is concluded that this effect is probably caused by a difference in heat capacity between the two phases. The observed results show, that temperature controlled atomic force microscopy complements the classical calorimetric experiments with the advantage of providing structural information on the nanometer scale. Thermodynamic data can be obtained by simple image processing methods from topographies at different temperature. The observed significant decrease of the main transition temperature by heptanol supports the assumption, that heptanol can regulate gap junctional coupling by fluidization of the lipid core adjacent to the cell-to-cell channels of gap junctions.

From the studies described so far, it becomes obvious that imaging of biological samples requires advances in technique and methodology to achieve routinely sub-molecular resolution of native or even living biological objects. One imaging mode, the so called *tapping mode*TM, is frequently applied to analyze soft biological samples and accounts for a reduction of lateral dragging forces. It is based on the oscillation of the force sensor's cantilever, which is excited by vibrating the measurement chamber near the cantilever's eigenfrequency. However, this method may also lead to unwanted and resolution limiting oscillation of the sample support and other peripheral parts of the set up. This may be improved by implementation of a new excitation scheme for the tapping mode [5]. It employs a commercial force sensor, whose metallic coating was selectively removed by a femtosecond-laser based high resolution micro structuring system. By this preparation, an oscillating current can be directed through the cantilever leading to a direct excitation by Lorentz force if the cantilever is placed in a static

magnetic field. By means of the measured response function of the microscope, it may be expected that an oscillation of the sample support and the sample can be significantly reduced by this technique in fluid as well as in air. The response function resembles that of a driven damped harmonic oscillator, except for a second peak at half of the eigenfrequency of the cantilever at fluid environment. This peak was identified to be caused by a temperature oscillation of the cantilever, which is induced by the alternating electrical current in the metallic coating. It can be concluded that this method has the potential to be implemented in future atomic force microscopes in order to achieve high resolution non-contact measurements in fluid environment.

In summary, the work presents the results of elucidation of the structure of biological membranes and proteins at fluid environment by atomic force microscopy. Starting at the topographical mapping of living intact cells the conclusion was drawn, that imaging at molecular resolution of whole cells under *in situ* conditions is difficult to achieve. The mica supported tonoplast was selected as a model system representing a native membrane which provided improved imaging conditions. The most abundant protein of the vacuolar membrane, the cytoplasmatic V_1 -part of the H^+ -ATPase was indirectly identified by a correlation algorithm and characterized by the spatial dimensions. But the resolution was still limited. However if proteins are available as crystalline array, even dynamic measurements are possible at molecular resolution providing new insights into the physicochemistry of protein crystallization. Temperature controlled atomic force microscopy of a supported bilayer made from a pure phospholipid allowed to determine important thermodynamic properties of the fluid to gel phase transition by image processing of structural data. For the first time, the cooperative unit of lipid phase transition was obtained from

structural data. The effect of the alcohol heptanol on bilayer structure and phase transition temperature was monitored which strongly support the assumption, that the physiological effects of heptanol on gap junctional cell-cell communication are mediated by modification of lipid rafts. In order to improve high resolution imaging of soft biological samples a Lorentz force based excitation method for tapping mode imaging was implemented. The force sensors were preprocessed by a laser based microstructuring unit allowing a batch production for daily routine. Although imaging of single membrane proteins in membranes of living cells still remains a challenge, the results obtained so far provide the perspective to elucidate the interaction of membrane proteins and the surrounding lipid bilayer with special consideration of lipid rafts. Submolecular resolution of the gating mechanisms of proteins might be achieved, if the protein is assembled as a regular two or three dimensional array which is the case for e.g. cell-to-cell channels of gap junctions. For this purpose a temperature control of the biological sample is of particular importance. At present, effects of signal molecules like cd95 or acidic sphingomyelinase on native or reconstituted lipid rafts are studied with molecular detail, from which the molecular mechanism of lipid raft signaling may be deduced in the future.

List of peer reviewed publications

- [1] H.-A. Kolb, O. Enders, and R. Schauer, 1999. Morphology of native and reconstituted biological membranes and their components analysed by atomic force microscopy. *Appl. Phys. A*, 68(2):247–254.
- [2] O. Enders, E. Martinoia, C. Zeilinger, and H.-A. Kolb, 2001. Identification of membrane proteins imaged by atomic force microscopy using a template matching algorithm. *Chinese Phys.*, 10:S100–S107.
- [3] M. Wiechmann, O. Enders, C. Zeilinger, and H.-A. Kolb, 2001. Analysis of protein crystal growth at molecular resolution by atomic force microscopy. *Ultramicroscopy*, 86(1-2):159–166.
- [4] O. Enders, A. Ngezahayo, M. Wiechmann, F. Leisten, and H.-A. Kolb, 2004. Structural calorimetry of main transition of supported DMPC bilayer by temperature controlled AFM. *Biophys. J.*, accepted.
- [5] O. Enders, F. Korte, and H.-A. Kolb, 2004. Lorentz force induced excitation of cantilevers for oscillation-mode scanning probe microscopy. *Surf. Interf. Anal.*, 36:119–123.

4 Morphology of Native and Reconstituted Biological Membranes and their Components Analysed by Atomic Force Microscopy

H.-A. Kolb^α, O. Enders^α and R. Schauer^α

^α Institute of Biophysics, University Hannover, Herrenhäuser Str. 2, D-30419 Hannover, Germany

Applied Physics A - Materials Science & Processing vol. 68 no. 2 p.
247-254, 1999

Copyright (1999) Springer. Reprinted with permission.

Abstract

The atomic force microscope can image the three-dimensional surface structure of soft biological membranes and their components in a physiological environment. Living macrophages prior to and after particle phagocytosis allowed low-resolution images by AFM. An active change of cell shape by mechanical stimulation is observed. Indentation depths of 1-30 nm were derived as function of cell preparation. High-resolution images were achieved for TexasRed IgG antibodies specifically bound to a mica-supported planar phospholipid bilayer doped with phospholipids containing headgroups of TexasRed. The cloned nicotinic acetylcholine receptor (nAChR) expressed in *Xenopus* oocytes were imaged at molecular resolution. An unambiguous identification of individual single nAChR proteins is hindered by the presence of endogenous membrane proteins. For the first time we introduce a favorable membrane system: the vacuolar membrane of plant cells, which allows the molecular identification of integral endogenous membrane proteins and a structural analysis of the lipid matrix.

4.1 Introduction

In 1986 the high-resolution imaging techniques were supplemented by the atomic force microscope (AFM) [6, 59], which is also called scanning force microscope (SFM). This technique offers the capability not only to investigate dried or fixed samples in vacuum, but allows us to examine the topography of samples in aqueous solutions containing physiological concentrations of salts at room temperature [12, 42]. Under most favorable conditions atomic resolution can be achieved on

hard samples [41, 43, 49, 65]. On soft biological samples submolecular resolution of some or even less than nm was achieved on 2D crystalline structures of proteins [48]. Large single molecules such as DNA fragments or enzymes can be quite easily distinguished [5] and even be watched at work [54]. The progress in high-resolution atomic force microscopy in biology was reviewed in [22, 35, 62]. But not only high-resolution imaging results in new insights into the structure of biological molecules. Also membrane surfaces and cytoskeletal components of whole and living cells could be imaged [10, 21, 24, 25] as well as biological processes on a cellular level such as the infection of MDCK cells by pox viruses [20, 50]. Some other biological cells and organelles should be mentioned: human platelets [56], glial cells [26, 61], MDCK cells [1, 30], magnetotactic bacteria [16], atrial myocytes [63], embryonic carcinoma cells [19], and cholinergic synaptic vesicles [40].

The atomic force microscope can be used in different ways. The most common one is the measurement of the topography of the samples. The determination of mechanical properties such as the local elasticity is also possible for appropriate sample systems [7, 55, 57, 66]. Biochemistry profits from the measurements of the binding force between specific interacting molecules such as biotin and avidin [15, 45] and within molecules such as titin [58].

Our studies were focused on imaging biological membranes during cellular activities such as phagocytosis by AFM. In addition, we are interested in revealing the topography of membrane lipids and proteins at low and high resolution as well as their specific identification in their native environment. The use of membranes has the advantage of limiting the sample movement, since the intermolecular interactions by preferential van der Waals forces and Coulomb force help to keep

the individual molecules in large ordered aggregates. The fixation of the sample is necessary for high image resolution, since it should not be able to move even a few Å. This approach was applied to reconstituted supported phospholipid bilayers with adsorbed specific antibodies as well as plasma membranes of *Xenopus laevis* oocytes expressing the nicotinic acetylcholine receptor channel complex. For the identification of endogenous integral membrane proteins at molecular resolution a new promising membrane system is introduced, the vacuolar membrane of plant cells.

4.2 Results and discussion

4.2.1 AFM images of living murine peritoneal macrophage

Atomic force microscopy in contact mode, that is the so-called repulsive force regime between tip and sample, has been used to profile the topography of the cell surface of living murine peritoneal macrophages. After isolation of macrophages from the peritoneum of mice, the cells were suspended on glass coverslips. The macrophages become spontaneously adherent.

Fig. 4.1 shows a time series of AFM images typical for a living macrophage adherent to a glass coverslip. The series shows the locomotion of the macrophage on the glass surface which accounts to several μm within an hour. Surprisingly, the figure indicates that the scanning tip perturbs the membrane surface initiating a specific cellular process, which results in a dramatic change in cell shape. Within the recorded time scale the center of the macrophage becomes significantly elevated. This is a remarkable phenomenon and resembles the stimulation of a nonspecific recognition mechanism in phagocytes

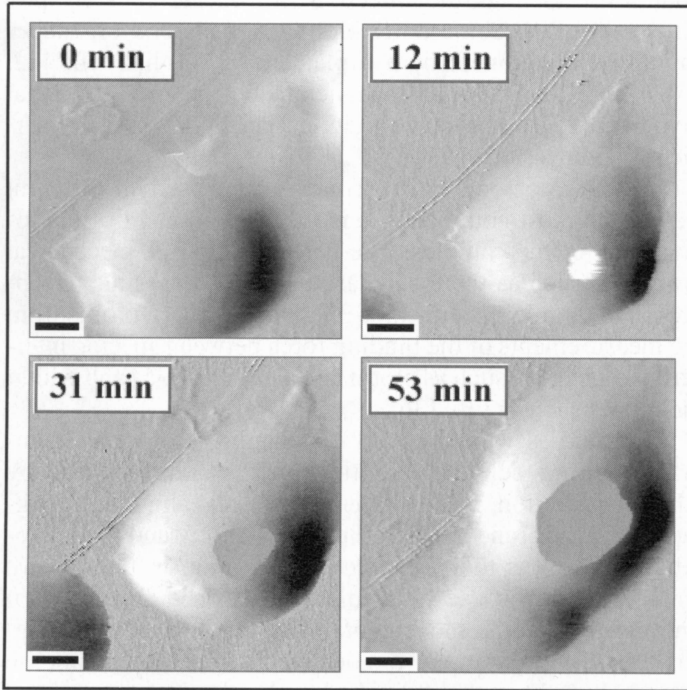


Figure 4.1: Series of AFM images in contact mode of an untreated, isolated living murine peritoneal macrophage adherent to a glass coverslip in physiological phosphate buffer solution. The recording times are indicated. The bar denotes $1 \mu\text{m}$, the total scan size is $7 \mu\text{m} \times 7 \mu\text{m}$. The isolation procedure has been described recently [2]. The flat area on the top of the cell is an artefact due to the maximum height out of range of the cantilever and of the z-piezo. The images were recorded using a commercial TMX 2010 (TopoMetrix, Santa Barbara, CA). The commercial software was used for leveling and shading the image with simulated light from the left. Imaging parameters: scan speed: $23 \mu\text{m/s}$, V-shaped cantilever with spring constant of 0.064 N/m ; loading force $\approx 1 \text{ nN}$.

[70] that is transduced by a putative mechanical sensor in the membrane [72]. Compared to particle phagocytosis [38] the interaction of the antibodylike tip with the cell surface is transient. It appears to be obvious that the indenting tip perturbs the architecture of the cytoskeleton, which initiates the observed cellular response. To elucidate the mechanism of particle phagocytosis we analysed particle phagocytosis by AFM. As particles we used latex beads with a diameter of about $0.45 \mu\text{m}$. It is known that macrophages phagocytose the antibodylike beads [2], which are related to changes of ion transport activities in the membrane [37] and the shape of the macrophage [72]. After addition of the beads to the bath phagocytosis occurs within minutes. Fig. 4.2a shows an image of a rim area of the macrophage after the beads had been washed off from the bath. Pseudopodia and incorporated beads can be seen as protrusions, but the actual endocytotic process could not be resolved. This is probably caused by the limited time and spatial resolution. Time resolution is in the range of 70-100 s. Lateral resolution is limited by the indentation of the tip into the soft, deformable cell body which amounts to several nm.

The indentation by the loading force is analysed in fig. 4.2b. The figure shows a membrane area after the first (image at upper right) and the fifth scan (image in the center). As can be read from the corresponding height profiles on the left the relief-like structures of membrane-covered latex beads become significantly pronounced. The images indicate that repetitive scanning indented the membrane between the beads by a factor of about 13. For comparison in the lower part of fig. 4.2b the image and height profile of pure latex beads are given.

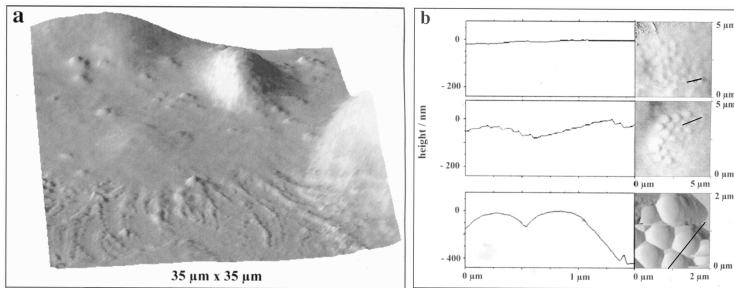


Figure 4.2: AFM topography of membrane areas of a living murine peritoneal macrophage after particle phagocytosis of latex beads with a diameter of $0.45 \mu\text{m}$ in physiological phosphate buffer solution. The macrophage is adherent to a plastic petri dish. For experimental details see [2]. a, shaded three-dimensional presentation of a rim area of $35 \mu\text{m} \times 35 \mu\text{m}$. Pseudopodia and membrane covered latex beads are visible. b, the right-hand side shows in the top(middle) image the topography of a central membrane area ($5 \mu\text{m} \times 5 \mu\text{m}$) after the first(fifth) scan process. For comparison the image at the bottom shows the topography of the pure latex beads adsorbed to a plastic petri dish. On the left-hand side height profiles are presented along the drawn line of $1.5 \mu\text{m}$, which are given in the corresponding topography on the right side. For the imaging parameters see fig. 4.1.

4.2.2 Force curves on peritoneal macrophages

Besides the topography some of the mechanical properties can be determined by atomic force microscopy. The elasticity can be quite easily determined by the use of an appropriate model such as the Hertz model [27, 66]. To gather the information that is necessary for the application of these models it is necessary to take so-called force curves [53]. The tip is moved uniformly downward until it comes so close to the sample that a repulsive force due to the orbital overlap between the tip and sample atoms dominates all other forces. The tip is mounted on a soft cantilever and will not penetrate the material except for extraordinary soft materials but indent the sample and will be deflected as the distance between the cantilever and sample reduces. The deflection can be converted to a force by the spring constant of the cantilever, which acts as a spring. The force is recorded during the approach and retraction of the tip. Such force curves can be seen in fig. 4.3.

Far away from the sample the tip is not deflected. This results in a straight horizontal line. Due to the attractive van der Waals force the tip is attracted to the sample if the medium does not reduce this interaction significantly. A sudden jump to contact, as shown in the inset, appears when the force gradient exceeds the spring constant. Then the tip gets in touch with the sample resulting in a infinite slope. Depending on the medium used different types of forces are more or less pronounced. In the experiments, denoted as A, B, and C in fig. 4.3, the solution was a physiological buffer containing a salt concentration of about 100 mM that screens the electrostatic interaction between the tip and the sample. The characteristic length scale for this screening, the Debye length, is less than 1 nm. The range of the other important

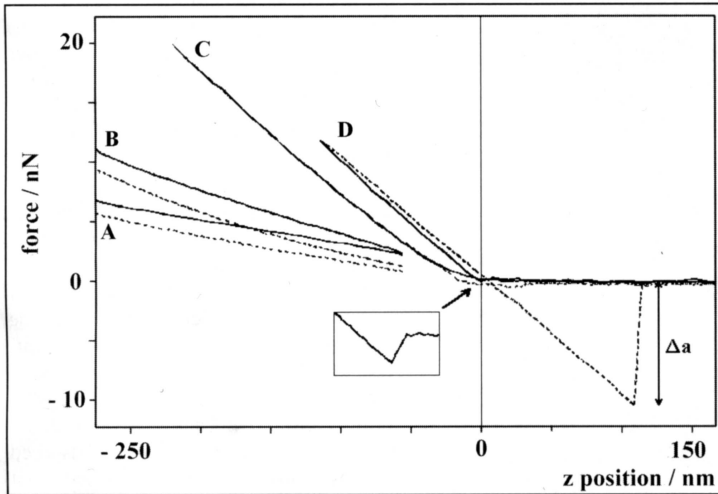


Figure 4.3: Force curves obtained at a randomly selected central elevated membrane location of adherent murine peritoneal macrophages as function of pretreatment and fixation. A, untreated macrophage in physiological phosphate buffer solution. B, macrophage after particle phagocytosis of latex beads in physiological phosphate buffer solution. C, macrophage after particle phagocytosis (see B) and fixation by addition of 1% glutaraldehyde to the physiological phosphate buffer solution. D, the macrophage was treated as described for C, but finally the adherent macrophage was air dried. The inset shows on a magnified scale ($30\times$) the so-called point of contact (in the absence of tip deformation, $z = 0$) [32]. Δa indicates the attractive pullout or adhesion force. At aqueous condition (see traces marked as A, B and C) the point of contact could not be measured (see text). The uncertainty in $z = 0$ is quite small, a few nm, compared with the distance over which the data were taken. The loading force was derived by the obtained cantilever deflection multiplied by its spring constant of 0.032 N/m . The drawn curves trace the cantilever loading force as the distance between sample and cantilever is reduced. The broken curves trace the cantilever loading force as distance increases. The time needed for a complete circle was about 1 s.

contribution, the van der Waals force, typically decays within a distance of some tens of nm. Neither force is relevant here. The tip will be in direct contact with the glycocalyx of the macrophage surface. The different slopes in fig. 4.3 result from the different stiffness of the macrophages that were prepared by various methods as indicated in the figure legend. The stiffer the material the higher is the absolute value of the slope approaching a maximum for an infinitely hard material that cannot be indented at all. During retraction the tip may stay in contact with the sample. As the cantilever continues to move upwards it will be bent downwards until the force exceeds a characteristic value. This force is defined as adhesion force Δa . It appears clearly for the dried macrophage in fig. 4.3, D and can be attributed to the meniscus forces [71]. The amount of the adhesion force depends on many experimental conditions that may be very difficult to control such as the cleanliness of the tip, the medium between tip and sample (especially air or liquid), and others, but was typically about 10 nN in these experiments. In liquid, capillary forces are no longer present (see fig. 4.3, trace A,B,C). A hysteresis in the curves reflects the plastic properties of the sample at low velocity of the tip movement [28]. In general it depends on the velocity with which the tip is moved. For high velocities a hydrodynamic drag appears depending on the viscosity of the medium [56]. The force curves of fig. 4.3 were taken at central points of a macrophage where its height was about 1 μm . The combined system of the cantilever and the macrophage can be modeled as a combination of two springs. The spring constants for differently prepared macrophage membrane were estimated for a given cantilever spring constant of 0.036 N/m to about 2 mN/m for a living untreated macrophage and 130 mN/m for an air-dried macrophage with phagocytosed latex beads [3]. These values are similar to those

found at the apical surface of a cultured MDCK cell monolayer [30]. The indentation depth for an applied force of 1 nN was about 30 nm in the first and about 6 nm in the latter case.

4.2.3 Reconstituted mica-supported phospholipid bilayers

The results of these studies indicate that the morphology of the membrane surface of living cells cannot be imaged at molecular resolution, which is mainly caused by the loading force yielding a significant elastic indentation of several nm as well as by the cell migration during the recording time. To be able to resolve membrane components at molecular resolution in aqueous solution it is necessary to use flat solid supported membrane layers. The simplest system for topographical images is the reconstituted planar lipid bilayer, especially of lipids in the gel phase in which the lipid molecules are essentially laterally immobile [8, 13, 14, 22, 29, 44, 60, 73, 74, 75]. Two methods are used to reconstitute planar phospholipid bilayers, the Langmuir-Blodgett method and the vesicle fusion technique. With respect to molecular resolution by AFM, this approach has been successfully applied for Langmuir-Blodgett films of phosphatidylethanolamine [64, 75], phosphatidylcholine [31], phosphatidylglycerol [13]. Recently the vesicle fusion technique [9] was used for the formation of phospholipid bilayers of diC15-PC¹ [4].

For the data presented in figs. 4.4 and 4.5 we used the vesicle fusion method. The vesicles contained a mixture of 80% diC15-PC, 20% diC15-PG² and in addition 2% TexasRed-DHPE³ (see legend of fig. 4.4 for experimental details). Since diC15-G is a negatively

¹1,2-pentadecanoyl-sn-glycero-3-phosphatidylcholine

²1,2-dipentadecanoyl-sn-glycero-3-phosphatidylglycerol

³N-(TexasRed sulfonyl)-1,2-dihexadecanoyl-sn-glycero-phosphoethanolamine

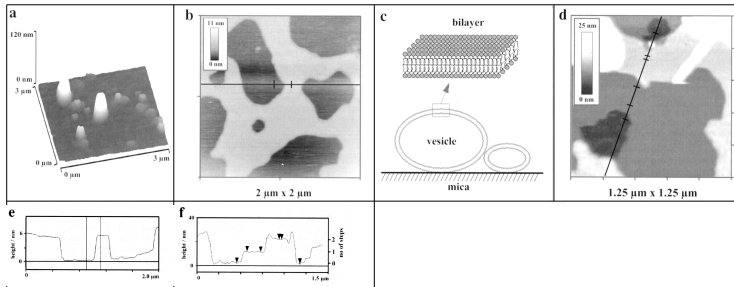


Figure 4.4: Effect of Ca^{2+} on the formation of mica-supported phospholipid bilayers in aqueous solution explored by AFM images in contact mode. The phospholipid bilayers explored were formed by the vesicle fusion method adopted from [9] as described elsewhere [4]. Briefly, the vesicle preparation contained a mixture of 80% diC15-PC and 20% diC15-PG (Avanti Polar Lipids Inc., Alabaster, AL) and 2% Texas-Red DHPE (Molecular Probes, Eugene, OR) suspended in the incubation solution of 500 mM NaCl, 20 mM Tris-HCl at pH 7.4. The vesicle suspension was placed on freshly cleaved mica and kept for 3h at 45° C, i.e. above the phase transition temperature of 33° C. All images were taken in the incubation solution at room temperature. a Gathered in the absence of Ca^{2+} with a NanoScope IIIa, MultiMode AFM (Digital Instruments, Santa Barbara, CA). Imaging parameters: scan size: 3 $\mu\text{m} \times 3 \mu\text{m}$, scan speed: 37 $\mu\text{m}/\text{s}$, spring constant of cantilever: 0.01 N/m, imaging force about 0.2 nN. Adsorbed vesicles with a diameter up to about 100 nm are clearly visible (a schematic view of the vesicles is given in c). b, d Spread planar phospholipid bilayers. 20 mM CaCl_2 was added to the incubation solution to initiate fusion of the negatively charged vesicles. b was recorded with a commercial TMX 2010 (see legend of fig. 4.1). Imaging parameters: scan size: 2 $\mu\text{m} \times 2 \mu\text{m}$, scan speed: 40 $\mu\text{m}/\text{s}$, cantilever spring constant: 0.032 N/m, loading force: ≈ 0.8 nN. d: was recorded with a NanoScope IIIa (see above). Imaging parameters: scan size: 1.25 $\mu\text{m} \times 1.25 \mu\text{m}$, scan speed: 10 $\mu\text{m}/\text{s}$, cantilever spring constant: 0.01 N/m, loading force: ≈ 0.2 nN. Non-ruby V-1 muscovite mica was a gift from S&J Trading (New York, N.Y.). e, f Height profiles along the lines in b, d respectively.

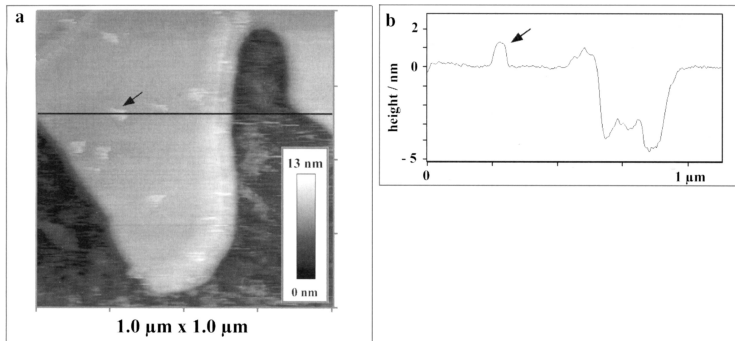


Figure 4.5: AFM image of a mica-supported doped phospholipid bilayer in electrolyte solution (see legend of fig. 4.4). a AFM image obtained in contact mode after addition of 50 μg AntiTexasRed rabbit IgG per ml incubation solution. (antiTexasRed rabbit IgG was purchased from Molecular Probes, Eugene, OR). The image was obtained about 10 min after addition of the antibody to the incubation solution (500 mM NaCl, 20 mM Tris-HCl at pH 7.4) using a NanoScope IIIa (see fig. 4.4). Imaging parameters: scan size: 1.2 μm \times 1.2 μm , scan speed: 8 $\mu\text{m}/\text{s}$, cantilever spring constant: 0.01 N/m, loading force: \approx 0.2 nN. b Height profile corresponding to the drawn line in a.

charged phospholipid the effect of Ca^{2+} on the vesicle fusion process could be studied. Fig. 4.4a shows that in the absence of Ca^{2+} vesicles adsorb to the mica surface, but do not fuse during the incubation period. Vesicles with diameters of up to 100 nm could be identified. Addition of 20 mM Ca^{2+} to the incubation solution accelerates the fusion process and areas of a spread planar phospholipid bilayer become visible (fig. 4.4b,d). The step size between the mica surface and the bilayer surface allows an estimation of the thickness of the lipid bilayer. It turns out that the derived height of about 5 nm (see fig. 4.4e,f), which includes the thickness of the thin hydration layer between the hydrophilic mica surface and the lower bilayer surface of about 1 nm [33, 36], underestimates the expected thickness of 5 nm for this phospholipid bilayer [67]. An electrostatic interaction between tip and sample should not contribute to this discrepancy [47], since the used high ionic strength of the incubation solution screens electrostatic forces. It seems to be more likely that even the applied low loading force of about 0.2 nN induces this deviation. Occasionally, multilayers were obtained by vesicle fusion in the presence of Ca^{2+} (see fig. 4.4d). Height profiles of the multilayers allowed a comparison of the derived step sizes. As the corresponding height profile indicates (fig. 4.4f) the mean step size slightly increases from 4.9 nm for the step between mica and the first bilayer to a mean of 5.2 nm for the second step between bilayer one and two. Further investigations are necessary to elucidate whether this increase in step size is caused by hydration layers of different thickness between the different surfaces.

We added an antiTexasRed rabbit IgG antibody to the incubation solution after a spread planar phospholipid bilayer had been formed by vesicle fusion. Fig. 4.5a shows a typical topographical image in contact mode about 10 min after the antibody had been added. The addition

of the antibody causes the appearance of significantly elevated spots on the bilayer surface that could not be observed in the absence of the antibody. From the corresponding height profiles (fig. 4.5b) a height of 1.5 ± 2.5 nm was estimated. This height is significantly smaller than observed for the TexasRed antibody adsorbed to freshly cleaved mica. In the latter case a height of 3.5 nm to 4.0 nm was derived, which is close to the expected value [23]. This variation could be caused by a partial incorporation of the bound antibody into the bilayer interface. The expected density of bound antibody should be larger by about one order of magnitude. These findings will be discussed in more detail by Schauer, Enders, and Kolb (in preparation).

The present results indicate that molecular resolution can be achieved for proteins specifically adsorbed to planar bilayers. In addition we analysed integral membrane proteins in native cell membranes at molecular resolution. A major problem arises from the identification of the type of an individual membrane protein within the ensemble of endogenous membrane proteins. To minimize the problem of identification, the membrane protein under consideration was overexpressed in the plasma membrane of *Xenopus laevis* oocytes.

4.2.4 AFM images of nicotinic acetylcholine receptor complexes expressed in *Xenopus* oocytes

The nicotinic acetylcholine receptor (nAChR) channel at the neuromuscular junction is the bestcharacterised member of a family of neurotransmitter-gated ion channels [17]. It is composed of a ring of five membrane-spanning subunits, which form a pentameric structure with a central cation conducting pathway [68]. The *Xenopus* oocyte expression system offers the possibility to identify the presence of func-

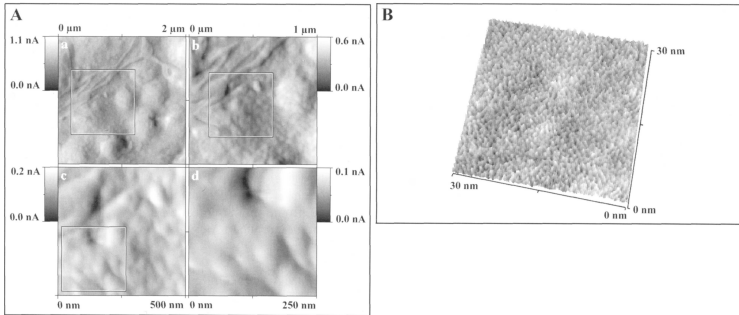


Figure 4.6: AFM images of defolliculated and air-dried patches of a *Xenopus laevis* oocyte membrane at lower and high resolution. The oocyte was either untreated (control condition) or previously injected with mRNA for expression of nicotinic acetylcholinereceptor (nAChR) (see [3]). a Image series of control oocyte with true magnification in contact mode. Imaging parameters: scan size was decreased by a factor of two from $2\ \mu\text{m} \times 2\ \mu\text{m}$ to $250\ \text{nm} \times 250\ \text{nm}$, scan speed: $10\ \mu\text{m}/\text{s}$, cantilever spring constant: $0.032\ \text{N}/\text{m}$, loading force: $\approx 1\ \text{nN}$. b High-resolution image of a control oocyte membrane recorded in tapping mode as 3D-presentation. Imaging parameters: scan size: $30\ \text{nm} \times 30\ \text{nm}$, scan speed: $15\ \mu\text{m}/\text{s}$, resonance frequency: $280\ \text{kHz}$.

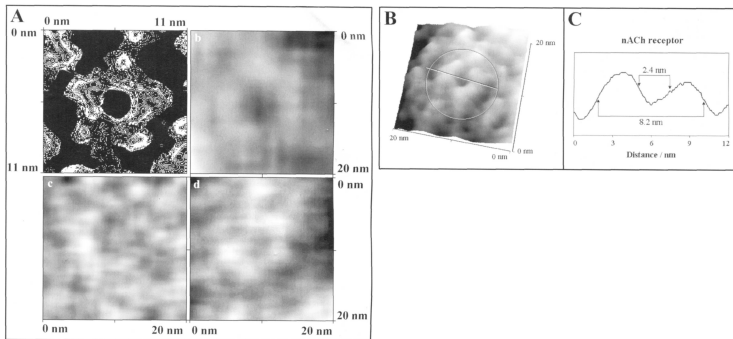


Figure 4.7: High-resolution images of nicotinic acetylcholine receptor (nAChR). a High-resolution images of oocyte membrane in contact mode. c Image of an oocyte membrane at control condition. b, d After expression of nAChR. Imaging parameters: scan speed: $10 \mu\text{m}$, cantilever spring constant: 0.032 N/m , loading force: $\approx 1 \text{ nN}$. For comparison (a) shows the result of the Fourier-enhanced EM investigations of nAChR by Unwin (1993) [68]. B Image given on the upper right in a in 3D presentation. The typical pentameric pattern is encircled. C Height profile corresponding to the straight line drawn in B. The error signal [51] is presented, respectively, using a TMX 2010 (see legend of fig. 4.1).

tionally intact acetylcholine sensitive nAChR channels by measuring the macroscopic conducting properties of the oocyte membrane by voltage clamp [11] prior to imaging.

Fig. 4.6a shows an image series of the membrane surface of a control oocyte with true magnification. Prior to imaging the membrane had been cut off the animal pole of the *Xenopus* oocyte, spread on a glass coverslip and air-dried. This preparation was necessary to achieve molecular resolution, since it turned out that the applied load of about 1 nN caused an indentation of the tip into the membrane of about 100 nm in aqueous solution. The series shows a smooth surface which becomes structured for scan sizes less than $100 \text{ nm} \times 100 \text{ nm}$ (see fig. 4.6b). It is striking that this high-resolution image of the oocyte membrane, which was processed in tapping mode [5, 22, 51, 54], resembles closely the corresponding image obtained on mica-supported reconstituted phospholipid bilayers [4]. The characteristic diameter of a single protrusion in fig. 4.6b is about 1 nm extruding 0.1 nm.

It is tempting to suggest that this pattern is formed by the head groups of lipid molecules in the oocyte membrane. Fig. 4.7a shows representative surface images of the oocyte membrane after expression of the nAChR channel (see also [3]). At molecular resolution various membrane structures could be identified on different oocytes. Images which indicate a pentameric structure as well as those without any symmetry were observed. The latter was obtained on an untreated control oocyte. The upper left drawing in fig. 4.7a shows a section crossing the extracellular part of nAChR in the closed configuration obtained from Fourier-enhanced EM investigations of nAChR by Unwin [68, 69]. In fig. 4.7b a 3D-presentation of the image in fig. 4.7a is shown wherein a typical pentameric pattern was identified.

From the corresponding height profile of this structure the diameter of the putative nAChR channel protein (8.2 nm) as well as the size of the central pore (2.4 nm) can be estimated. Both values closely resemble the results found by Lal [39], but are systematically larger than reported by Unwin [68]. The difference might be caused by the convolution of the tip and the sample. It has to be emphasised that an unambiguous identification of the presented pentameric structure as nAChR channel is not possible. This identification is a general problem for individual membrane molecules that are not ordered in a lattice (cf. [46]). Labelled markers would support an identification, but usually modify and trap the identified structure in high-resolution images. Furthermore, the topography of endogenous membrane proteins is not known.

For AFM studies of endogenous integral membrane proteins in native cell membranes in aqueous solution we selected a favorable system, the vacuole membrane of plant cells.

4.2.5 AFM images of the two vacuolar membrane interfaces

Lateral resolution depends mainly on the contact area between tip and sample. As shown above in the case of native living macrophages indentation depths of several nm leads to a contact area of several nm², even if the tip radius is in the order of 10 nm and the imaging force well below 1 nN. In addition membrane structures are moved laterally by friction forces between tip and sample, prohibiting molecular resolution. To be able to image membrane proteins with molecular resolution under in situ conditions the membrane has to be fixed to a flat and rigid substrate to resist significant indentation of the scanning tip at low imaging forces. Therefore it is necessary to spread

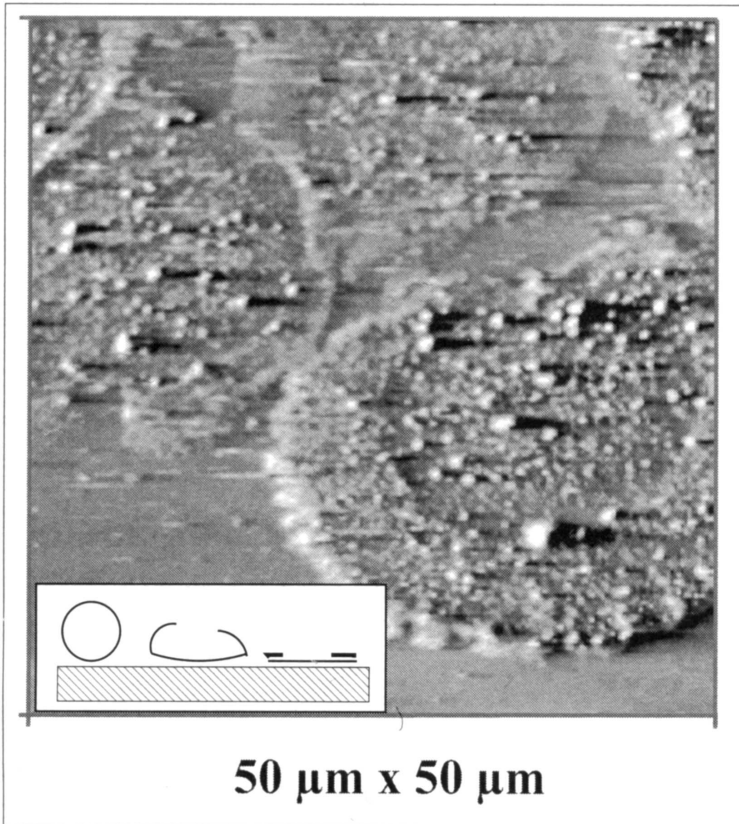


Figure 4.8: AFM image in contact mode of vacuolar membrane of barley leaves spread on mica recorded in aqueous solution. Vacuoles of barley leaves were isolated as described previously [34]. Briefly, the vacuoles were isolated from barley mesophyll protoplasts by differential centrifugation and were added as suspension in an electrolyte solution (0.4 mM betaine, 10 mM potassiumgluconate, 20 mM HEPES at pH 7.2) to the mica surface. Imaging parameters: scan size: 50 μm \times 50 μm , scan speed: 150 $\mu\text{m}/\text{s}$, cantilever spring constant: 0.032 N/m, loading force: \approx 1 nN. The error signal [52] using a TMX 2010 (see legend of fig. 4.1) is shown. The inset shows the modeled rupture process of a vacuole.

the cellular membrane patches on a solid support. But in general the spreading process does not occur spontaneously, due to the presence of the cytoskeleton. For this reason vacuolar membranes were chosen, which are free of cytoskeletal structures. Vacuoles belong to the most important organelles of the plant cell. They are surrounded by a membrane, the tonoplast, and contain an acidic vacuolar fluid and no significant amount of solid substances. The vacuoles can be isolated without secondary structures. The experiments show that isolated vacuoles adsorb spontaneously to freshly cleaved mica surfaces by electrostatic and van der Waals interaction. Due to the strong attractive interaction between the vacuolar membrane and the mica surface the attached spherical vacuoles rupture and the membrane adsorbs completely to the mica surface. Two membrane areas corresponding to the two membrane interfaces could be discriminated, a central adsorption area which exposes the intravacuolar side of the vacuolar membrane to the scanning tip, and a peripheral area near to the rim of the adsorbed vacuole membrane exposing the extravacuolar (cytoplasmic) side to the scanning tip (see inset in fig. 4.8). Both areas can be discriminated by their different heights of about 5 nm and 14 nm, respectively. This indicates that at the rim two membrane layers are on top of each other as shown in the inset in fig. 4.8. Since the thickness of the vacuolar membrane (tonoplast) is in the order of only 5-10 nm, the sample withstands the local pressure applied by the tip, and the contact area remains small, allowing similar resolutions as achieved for reconstituted bilayers.

Fig. 4.8 reveals a typical image of the adsorbed and ruptured vacuole. The image was obtained under aqueous condition. The aqueous solution was identical to that used for the isolation procedure and attachment of the vacuoles to the mica surface. The specific composi-

tion was chosen to conserve the functional activity of the vacuolar proteins. The figure shows a variety of protrusions above the membrane surface different in size, which we attributed to single and clustered membrane proteins. The major population of elevated structures exposing the cytoplasmic face of the membrane had a height of 12 nm to 14.5 nm. This dimension would correspond to the cytoplasmic orientated extramembraneous part of the major population of integral vacuolar membrane proteins, the VATPase [18]. In addition a few small vesicular structures are visible. The vesicles may emerge during the adsorption process, which could produce a local excess of lipids. The latter could be compensated by vesicle formation which are subsequently released from the membrane. These preliminary results present a native membrane system that allows high-resolution imaging of single-membrane proteins.

Further application will probably extend the use of atomic force microscopy to other potential biological and biotechnological applications, including functional and structural characterization and manipulation, real-time imaging of the kinetics of cellular processes and conformational changes, as well as quality control of biological devices such as biosensors and assays on the molecular level.

4.3 Conclusion

The presented AFM studies on wet native membranes reveal the difficulty in visualising the structure of individual lipids and proteins at molecular level. In the case of lipid molecules the softness of wet native membranes as well as the incorporated glycoproteins may hinder and screen the detection of single lipid head groups. Nevertheless, reconstituted, supported bilayer membranes and fixed native mem-

branes allow such resolution. Improvement of the used cantilever and tip and the technique of spreading wet native membranes will be necessary for true molecular resolution of membrane proteins simultaneously with membrane lipids. Yet, the identification and classification of individual proteins and lipids within their native environment still remains an unsolved challenge. Further application will probably extend the use of AFM to other potential biological and biotechnical applications, including functional and structural characterization and manipulation, real-time imaging of the kinetics of cellular processes and conformational changes, as well as quality control of biological devices such as biosensors and assays on the molecular level.

References

- [1] A-Hassan, E., W. F. Heinz, M. D. Antonik, N. P. D'Costa, S. Nageswaran, C. A. Schoenenberger, and J. H. Hoh, 1998. Relative microelastic mapping of living cells by atomic force microscopy. *Biophys. J.* 74:1564–78
- [2] Beckmann, M., H.-A. Kolb, and F. Lang, 1994. Atomic force microscopy of peritoneal macrophages after particle phagocytosis. *J. Membr. Biol.* 140:197–204
- [3] Beckmann, M., H.-A. Kolb, and F. Lang, 1995. Atomic force microscopy of biological cell membranes: From cells to molecule. *Eur. Microsc. Anal.* 1:5–7
- [4] Beckmann, M., P. Nollert, and H.-A. Kolb, 1998. Manipulation and molecular resolution of a phosphatidylcholine-supported planar bilayer by atomic force microscopy. *J. Membr. Biol.* 161:227–33
- [5] Bezanilla, M., B. Drake, E. Nudler, M. Kashlev, P. K. Hansma, and H. G. Hansma, 1994. Motion and enzymatic degradation of DNA in the atomic force microscope. *Biophys. J.* 67:2454–9
- [6] Binnig, G., C. F. Quate, and C. Gerber, 1986. Atomic force microscope. *Phys. Rev. Lett.* 30:355

-
- [7] Bottomley, L. A., J. E. Coury, and P. N. First, 1996. Scanning probe microscopy. *Anal. Chem.* 68:185–230
- [8] Brandow, S. L., D. C. Turner, B. R. Ratna, and B. P. Gaber, 1993. Modification of supported lipid membranes by atomic force microscopy. *Biophys. J.* 64:898–902
- [9] Brian, A. A. and H. M. McConnell, 1984. Allogeneic stimulation of cytotoxic T cells by supported planar membranes. *Proc. Natl Acad. Sci. U S A* 81:6159–63
- [10] Butt, H. J., E. K. Wolff, S. A. Gould, B. D. Northern, C. M. Peterson, and P. K. Hansma, 1990. Imaging cells with the atomic force microscope. *J. Struct. Biol.* 105:54–61
- [11] Dascal, N., 1987. The use of *Xenopus* oocytes for the study of ion channels. *CRC Crit. Rev. Biochem.* 22:317–87
- [12] Drake, B., C. B. Prater, A. L. Weisenhorn, S. A. C. Gould, T. R. Albrecht, C. F. Quate, D. S. Cannell, H. G. Hansma, and P. K. Hansma, 1989. Imaging crystals, polymers, and processes in water with the atomic force microscope. *Science* 243:1586
- [13] Egger, M., F. Ohnesorge, A. L. Weisenhorn, S. P. Heyn, B. Drake, C. B. Prater, S. A. C. Gould, P. K. Hansma, , and H. E. Gaub, 1990. Wet lipid-protein membranes imaged at submolecular resolution by atomic force microscopy. *J. Struct. Biol.* 103:89–94
- [14] Engel, A., 1991. Biological applications of scanning probe microscopes. *Annu Rev Biophys Chem* 20:79–108
- [15] Florin, E. L., V. T. Moy, and H. E. Gaub, 1994. Adhesion forces between individual ligand-receptor pairs. *Science* 264:415–7

-
- [16] Fritz, M., M. Radmacher, N. Petersen, and H. E. Gaub, 1994. Visualization and identification of intracellular structures by force modulation microscopy and drug induced degradation. *J. Vac. Sci. Technol. B* 12:1526–1529
- [17] Galzi, J. L., F. Revah, A. Bessis, and J. P. Changeux, 1991. Functional architecture of the nicotinic acetylcholine receptor: from electric organ to brain. *Annu. Rev. Pharmacol. Toxicol.* 31:37–72
- [18] Getz, H. P. and M. Klein, 1995. The vacuolar ATPase of red beet storage tissue - electron-microscopy demonstration of the head-and-stalk structure. *Bot. Acta* 108:14
- [19] Goldmann, W. H. and R. M. Ezzell, 1996. Viscoelasticity in wild-type and vinculin-deficient (5.51) mouse F9 embryonic carcinoma cells examined by atomic force microscopy and rheology. *Exp. Cell Res.* 226:234–7
- [20] Häberle, W., J. K. Hörber, F. Ohnesorge, D. P. Smith, and G. Binnig, 1992. In situ investigations of single living cells infected by viruses. *Ultramicroscopy* 42-44 (Pt B):1161–7
- [21] Häberle, W., J. K. H. Hörber, and G. Binnig, 1991. Force microscopy on living cells. *J. Vac. Sci. Technol. B* 9:1210–1213
- [22] Hansma, H. G. and J. H. Hoh, 1994. Biomolecular imaging with the atomic force microscope. *Annu. Rev. Biophys. Biomol. Struct.* 23:115–39

-
- [23] Harris, L. J., E. Skaletsky, and A. McPherson, 1998. Crystallographic structure of an intact IgG1 monoclonal antibody. *J. Mol. Biol.* 275:861–72
- [24] Haydon, P. G., R. Lartius, V. Parpura, and S. P. Marchese-Ragona, 1996. Membrane deformation of living glial cells using atomic force microscopy. *J. Microsc.* 182 (Pt 2):114–20
- [25] Henderson, E., 1994. Imaging of living cells by atomic-force microscopy. *Progr. Surf. Sci.* 46:39
- [26] Henderson, E., P. G. Haydon, and D. S. Sakaguchi, 1992. Actin filament dynamics in living glial cells imaged by atomic force microscopy. *Science* 257:1944–6
- [27] Hertz, H., 1882. über die berührung fester elastischer körper,. *J. Reine U. Angew. Math.* 92:156–171
- [28] Hoh, J. H. and A. Engel, 1993. Friction effects on force measurements with an atomic force microscope. *Langmuir* 9:3310 – 3312
- [29] Hoh, J. H. and P. K. Hansma, 1992. Atomic force microscopy for high resolution imaging in cell biology. *Trends Cell Biol.* 208–213
- [30] Hoh, J. H. and C. A. Schoenenberger, 1994. Surface morphology and mechanical properties of MDCK monolayers by atomic force microscopy. *J. Cell Sci.* 107 (Pt 5):1105–14
- [31] Hui, S. W., R. Viswanathan, J. A. Zasadzinski, and J. N. Israelachvili, 1995. The structure and stability of phospholipid bilayers by atomic force microscopy. *Biophys. J.* 68:171–8

-
- [32] Hutter, J. L. and J. Bechhoefer, 1992. Calibration of atomic-force microscope tips. *Rev. Sci. Instrum.* 64:1868–1873
- [33] Johnson, S. J., T. M. Bayerl, D. C. McDermott, G. W. Adam, A. R. Rennie, R. K. Thomas, and E. Sackmann, 1991. Structure of an adsorbed dimyristoylphosphatidylcholine bilayer measured with specular reflection of neutrons. *Biophys. J.* 59:289–94
- [34] Kaiser, G., E. Martinoia, and A. Wiemken, 1982. Rapid appearance of photosynthetic products isolated from barley mesophyll protoplasts by a new fast method. *Z. f. Pflanzenphys.* 107:103–113
- [35] Kasas, S., N. H. Thomson, B. L. Smith, P. K. Hansma, J. Miklossy, and H. G. Hansma, 1997. Biological applications of the AFM: From single molecules to organs. *Int. J. of Imag. Syst. And Techn.* 8:151
- [36] Koenig, B. W., S. Krueger, W. J. Orts, C. F. Majkrzak, N. F. Berk, J. V. Silverton, and K. Gawrisch, 1996. Neutron reflectivity and atomic force microscopy studies of a lipid bilayer in water adsorbed to the surface of a silicon single crystal. *Langmuir* 12:1336–1342
- [37] Kolb, H.-A. and J. Ubl, 1987. Activation of anion channels by zymosan particles in membranes of peritoneal macrophages. *Biochim. Biophys. Acta* 899:239–46
- [38] Kolb-Bachofen, V., 1992. Uptake of toxic silica particles by isolated rat liver macrophages (Kupffer cells) is receptor mediated and can be blocked by competition. *J. Clin. Invest.* 90:1819–24

- [39] Lal, R. and L. Yu, 1993. Atomic force microscopy of cloned nicotinic acetylcholine receptor expressed in *Xenopus* oocytes. *Proc. Natl Acad. Sci. U S A* 90:7280–4
- [40] Laney, D. E., R. A. Garcia, S. M. Parsons, and H. G. Hansma, 1997. Changes in the elastic properties of cholinergic synaptic vesicles as measured by atomic force microscopy. *Biophys. J.* 72:806–13
- [41] Lüthi, R., M. Bammerlin, and E. Meyer, 1997. Atomare Auflösung auf einem Isolator mittels Rasterkraftmikroskopie. *Phys. Blätter* 53:435
- [42] Marti, O., B. Drake, and P. K. Hansma, 1987. Atomic force microscopy of liquid-covered surfaces - atomic resolution images. *Appl. Phys. Lett.* 51:484
- [43] Meyer, G. and N. M. Amer, 1988. Novel optical approach to atomic force microscopy. *Appl. Phys. Lett.* 53:1045
- [44] Mou, J., J. Yang, and Z. Shao, 1994. Tris (hydroxymethyl) aminomethane (C₄H₁₁NO₃) induced a ripple phase in supported unilamellar phospholipid bilayers. *Biochemistry* 33:4439–43
- [45] Moy, V. T., E. L. Florin, and H. E. Gaub, 1994. Intermolecular forces and energies between ligands and receptors. *Science* 266:257–9
- [46] Müller, D. J., M. Amrein, and A. Engel, 1997. Adsorption of biological molecules to a solid support for scanning probe microscopy. *J. Struct. Biol.* 119:172–88

-
- [47] Müller, D. J. and A. Engel, 1997. The height of biomolecules measured with the atomic force microscope depends on electrostatic interactions. *Biophys. J.* 73:1633–44
- [48] Müller, D. J., C.-A. Schoenenberger, F. Schabert, and A. Engel, 1997. Structural changes in native membrane proteins monitored at subnanometer resolution with the atomic force microscope: A review. *J. Struct. Biol.* 119:149
- [49] Ohnesorge, F. and G. Binnig, 1993. True atomic-resolution by atomic force microscopy through repulsive and attractive forces. *Science* 260:1451
- [50] Ohnesorge, F. M., J. K. Hörber, W. Häberle, C. P. Czerny, D. P. Smith, and G. Binnig, 1997. AFM review study on pox viruses and living cells. *Biophys. J.* 73:2183–94
- [51] Putman, C. A., K. O. van der Werf, B. G. de Groot, N. F. van Hulst, and J. Greve, 1994. Viscoelasticity of living cells allows high resolution imaging by tapping mode atomic force microscopy. *Biophys. J.* 67:1749–53
- [52] Putman, C. A., K. O. van der Werf, B. G. de Groot, N. F. van Hulst, J. Greve, and P. K. Hansma, 1992. New imaging mode in atomic-force microscopy based on the error signal. *SPIE* 1639:198–204
- [53] Radmacher, M., M. Fritz, J. P. Cleveland, D. A. Walters, and P. K. Hansma, 1994. Imaging adhesion forces and elasticity of lysozyme adsorbed on mica with the atomic force microscope. *Langmuir* 10:3809–3814

-
- [54] Radmacher, M., M. Fritz, H. G. Hansma, and P. K. Hansma, 1997. Direct observation of enzyme activity with the atomic force microscope. *Science* 265:1577–1579
- [55] Radmacher, M., M. Fritz, and P. K. Hansma, 1995. Imaging soft samples with the atomic force microscope: Gelatin in water and propanol. *Biophys. J.* 69:264–70
- [56] Radmacher, M., M. Fritz, C. M. Kacher, J. P. Cleveland, and P. K. Hansma, 1996. Measuring the viscoelastic properties of human platelets with the atomic force microscope. *Biophys. J.* 70:556–67
- [57] Radmacher, M., R. W. Tillman, and H. E. Gaub, 1993. Imaging viscoelasticity by force modulation with the atomic force microscope. *Biophys. J.* 64:735–42
- [58] Rief, M., M. Gautel, F. Oesterhelt, J. M. Fernandez, and H. E. Gaub, 1997. Reversible unfolding of individual titin immunoglobulin domains by AFM. *Science* 276:1109–12
- [59] Rugar, D. and P. Hansma, 1990. Atomic force microscopy. *Phys. Today* 43:23–30
- [60] Sackmann, E., 1996. Supported membranes: Scientific and practical applications. *Science* 271:43–8
- [61] Schaus, S. S. and E. R. Henderson, 1997. Cell viability and probe-cell membrane interactions of XR1 glial cells imaged by atomic force microscopy. *Biophys. J.* 73:1205–14
- [62] Shao, Z. F. and J. Yang, 1995. Progress in high-resolution atomic-force microscopy in biology. *Quart. Rev. of Biophys.* 28:195

-
- [63] Shroff, S. G., D. R. Saner, and R. Lal, 1995. Dynamic micromechanical properties of cultured rat atrial myocytes measured by atomic force microscopy. *Am. J. Physiol.* 269:C286–92
- [64] Singh, S. and D. J. Keller, 1990. Atomic force microscopy of supported planar membrane bilayers. *Biophys. J.* 60:1401–1410
- [65] Sonnenfeld, R. and P. K. Hansma, 1986. Atomic-resolution microscopy in water. *Science* 232:211
- [66] Tao, N. J., S. M. Lindsay, and S. Lees, 1992. Measuring the microelastic properties of biological material. *Biophys. J.* 63:1165–9
- [67] Tardieu, A., V. Luzzati, and F. C. Reman, 1973. Structure and polymorphism of the hydrocarbon chains of lipids: a study of lecithin-water phases. *J. Mol. Biol.* 75:711–33
- [68] Unwin, N., 1993. Nicotinic acetylcholine receptor at 9 Å resolution. *J. Mol. Biol.* 229:1101–24
- [69] Unwin, N., 1995. Acetylcholine receptor channel imaged in the open state. *Nature* 373:37–43
- [70] Weir, D. M. and H. M. Ogmundsdottir, 1977. Non-specific recognition mechanisms by mononuclear phagocytes. *Clin. Exp. Immunol.* 30:323–9
- [71] Weisenhorn, A. L., P. Maivald, H.-J. Butt, and P. K. Hansma, 1992. Measuring adhesion, attraction, and repulsion between surfaces in liquids with an atomic-force microscope. *Phys. Rev. B* 45:11226–11232

- [72] Wright, S. D. and S. C. Silverstein, 1986. Overview: the function of receptors in phagocytosis. *In Cellular Immunology*, D. M. Weir, editor, 41.1–41.14. Blackwell Scientific Publications
- [73] Yang, J., L. K. Tamm, A. P. Somlyo, and Z. Shao, 1993. Promises and problems of biological atomic force microscopy. *J. Microsc.* 171 (Pt 3):183–98
- [74] Yang, J., L. K. Tamm, T. W. Tillack, and Z. Shao, 1993. New approach for atomic force microscopy of membrane proteins. The imaging of cholera toxin. *J. Mol. Biol.* 229:286–90
- [75] Zasadzinski, J. A., C. A. Helm, M. L. Longo, A. L. Weisenhorn, S. A. Gould, and P. K. Hansma, 1991. Atomic force microscopy of hydrated phosphatidylethanolamine bilayers. *Biophys. J.* 59:755–60

5 Identification of Membrane Proteins Imaged by Atomic Force Microscopy Using a Template Matching Algorithm

O. Enders ^{α} , E. Martinoia ^{β} , C. Zeilinger ^{α} , and H.-A. Kolb ^{α}

^{α} Institute of Biophysics, University Hannover, Herrenhäuser Str. 2, D-30419 Hannover, Germany

^{β} Institut de Botanique, Laboratoire de Physiologie Végétale, Rue Emile-Argand 13, CH-2007 Neuchatel, Switzerland

Published in: Chinese Physics vol. 10(S) pp. 100-8 (2001)
The article was not reprinted in the thesis because of copyright reasons.

6 Analysis of Protein Crystal Growth at Molecular Resolution by Atomic Force Microscopy

M. Wiechmann^α, O. Enders^α, C. Zeilinger^α, and H.-A. Kolb^α

^α Institute of Biophysics, University Hannover, Herrenhäuser Str. 2, D-30419 Hannover, Germany

^β Institut de Botanique, Laboratoire de Physiologie Végétale, Rue Emile-Argand 13, CH-2007 Neuchatel, Switzerland

^α Institute of Biophysics, University Hannover, Herrenhäuser Str. 2, D-30419 Hannover, Germany

Reprinted from *Ultramicroscopy* vol. 86(1/2), M. Wiechmann, O. Enders, C. Zeilinger, H.-A. Kolb, Analysis of Protein Crystal Growth at Molecular Resolution by Atomic Force Microscopy, pp. 156-66, Copyright (2001) with permission from Elsevier

Abstract

High-resolution AFM studies have been performed to analyze the molecularity of growth steps of the (110) face of tetragonal lysozyme crystals. Besides a major population of step heights of about 5.5 nm also step heights of about half this size were observed. The latter steps always appeared pairwise. Both surfaces the (110) face and the (101) face could be imaged at molecular level. Comparison of the height pattern of the corresponding surface structure indicates that the (110) face is relatively smooth of less than 1 nm compared to the (101) face of about 4.2 nm. AFM linescan images of the (101) face indicate rather the insertion of lysozyme aggregates in solution to the crystal surface than lysozyme monomers. This study suggests that insertion of lysozyme aggregates from the solution yield to growth steps of the (110) face of monomolecular as well as of bimolecular unit height.

6.1 Introduction

The tetragonal form of hen egg-white lysozyme [1, 2] continues to be the most investigated protein crystal for growth studies. With the invent of the atomic force microscopy (AFM) it became possible to directly observe growth kinetics and the structure of protein crystals under *in situ* conditions in aqueous environment. Processes as dislocation growth and two dimensional nucleation growth, especially the motion of growth steps have been studied [3, 4]. The growing of protein crystals could be followed by AFM up to molecular resolution [7, 18]. The present work is focussed to the analysis of two conflicting aspects of growth of tetragonal lysozyme crystals.

Concerning the molecularity of the growth steps of tetragonal lysozyme crystals it has been reported, that the (110) face proceeds always in bimolecular growth steps [3, 7]. In contrast Durbin & Feher, 1990 [5] and Nadarajah & Pusey, 1996 [14] proposed a growth in monomolecular layers. Such monomeric step have been reported for the (101) face [3]. In both cases the specific growth steps could be related to the maximum repeating unit in the specific direction [14], respectively.

In this study we explored the molecularity of the growth steps of the (110) face at supersaturation condition. In addition we addressed one important question whether the analyzed crystals grow by incorporation of monomeric molecules from bulk solution into the crystal lattice or whether multimeric units are built before they reach the incorporation site. For this purpose linescans across growth steps were performed at the (101) face.

6.2 Materials and methods

6.2.1 Sample preparation

Samples were placed on muscovite mica ($2 \times 2 \text{ mm}^2$), which was attached to a microscopic glass plate by an epoxy glue (Sylgard, Sylgard Corp.). The glass plate was glued to a metallic disc to fix the sample holder of the AFM scan unit.

Hen egg white lysozyme (Sigma-Aldrich, lot. no. L-6878) was two times dialyzed against bidistilled water and equilibrated with 50 mM sodium acetate (NaAc) buffer solution (pH 4.5). The final lysozyme concentration was determined by photometric adsorption spectrometry (Uvikon 932, Bio-Tek Kontron Instruments, Neufahrn, Germany) assuming an extinction coefficient of $\epsilon_{280} = 379351 \text{ mol}^{-1} \text{ cm}^{-1}$. Prior to the experiments, the lysozyme stock solution was mixed with water and the precipitation solution (10% NaCl (w/v), 50 mM NaAc, pH 4.5) to a final concentration between 3% and 4% (w/v) lysozyme and 3% (w/v) NaCl. A drop of this solution was placed on freshly cleaved mica.

Nucleation and generation of small crystals on the mica surface was initiated by storing the sample holder at 4° C for about 10 minutes. Further crystal growth occurred for a duration of several hours at room temperature. As soon as crystals could be identified of suitable shape and orientation by an optical microscope, the sample holder was mounted for imaging into the AFM.

6.2.2 Atomic force microscopy

A commercial atomic force microscope (Digital Instruments Multi-Mode AFM, Nanoscope IIIa controller and 1227 J-z scanner, Santa

Babara, CA, USA) equipped with a fluid cell was used for the experiments. Soft cantilever tips of force constants 0.02 N/m and resonance frequency 13 kHz were used (Olympus Optical, Tokyo, Japan). High-resolution images were acquired in contact mode with an imaging force below 500 pN, which was determined by force distance measurements. Parameters of the feedback loop, which sets the cantilever deflection, were adjusted to moderate values to yield a sufficient high contrast in deflection signal images.

After transferring the sample to the AFM, the fluid cell was filled with the crystallizing solution. The system was equilibrated for several minutes to about half an hour. Crystallizing conditions were maintained during all measurements.

Data post processing

The imaged crystal surfaces are tilted by angles of more than 20° against the xy-plane of the scanner. In order to detect and measure small height differences in the image data, the “plane fit” algorithm (supplemented with the commercial imaging software) was applied to the topographical data. This algorithm subtracts a fitted two-dimensional polynomial plane from the raw data, that the surface appears to be in parallel with the xy-plane. This causes a geometrical discrepancy between the measured and true height differences, which cannot be neglected at great tilt angles. The factor $f(\alpha)$ which accounts for the deviation can be derived from simple geometrical considerations as function of the tilt angle α :

$$f(\alpha) = \frac{1}{\cos(\alpha)}$$

The measured height values of growing planes were corrected by this factor.

Data are given as mean \pm s.e.m. and n denotes the number of independent measurements.

Linescan mode

In order to enhance the time resolution to be able to track insertion events of single proteins or protein clusters into the crystal, the linescan mode [8] was applied. In this mode, the tip senses one single line 128 to 512 times per image. The resulting images show the deflection or topographic signal of the linescan in x-direction and its time evolution in y-direction. At scan rates of about 10 lines/s events of growth could be observed at a time resolution below 0.1 s. A lateral drift was analysed by recording a step within the surface of freshly cleaved mica under wet conditions. The parameters of the linescan image were set to the values used for the corresponding linescan of tetragonal lysozyme crystal surface. A constant monotonic drift of typically less than 0.25 nm/s was obtained.

6.3 Results

6.3.1 Size and kinetics of growth steps of the (110) crystal face

Lysozyme crystallization was initiated as described in *Materials and Methods*. Macrocrystals were grown by incubating the sample support 18 h at room temperature (24° C). Crystals with dimensions of the order of several 100 μ m could be identified on the sample support by a video microscope which is combined with the atomic force microscope. Thereafter, the cantilever of the AFM was adjusted above a (110) surface of the tetragonal lysozyme crystal. The application

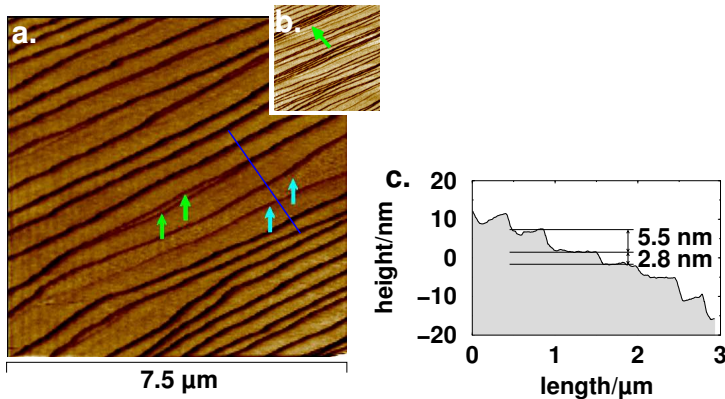


Figure 6.1: (a) Image showing the deflection signal of a (110) surface of a tetragonal lysozyme crystal at crystallization conditions. Step heights were measured from corresponding topographical data. Average heights of 5.5 nm were measured for the majority of steps. Pairs of steps with heights of about half this value were found (green/blue arrows) occasionally (scan rate: 224 $\mu\text{m/s}$). The inset represents deflection data showing macrosteps (green arrow) (scan rate: 224 $\mu\text{m/s}$). (b) Height profile along the straight line given in (a). A step of 5.5 nm and of 2.8 nm are marked, respectively.

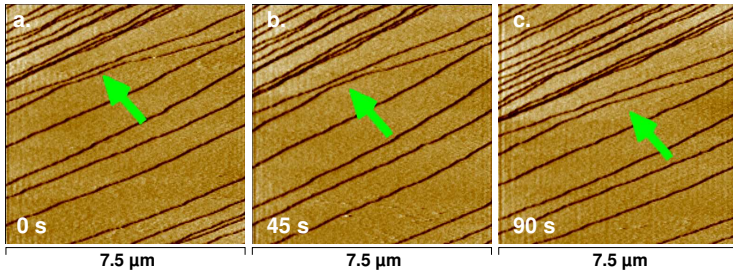


Figure 6.2: Sequence of images showing the deflection signal of a (110) surface of a tetragonal lysozyme crystal in crystallization conditions recorded at the given times. Growth steps move from upper left to lower right. The arrow marks a characteristic step pattern, which helps to determine the lateral step velocity (scan rate: $224 \mu\text{m/s}$).

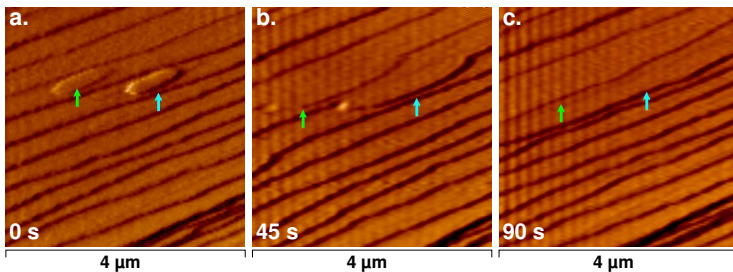


Figure 6.3: Sequence of deflection images showing two-dimensional nucleation on a (110)-surface (see arrows). The nuclei grow laterally (a and b) and fuse with neighboring growing terraces (c) (scan rate: $224 \mu\text{m/s}$).

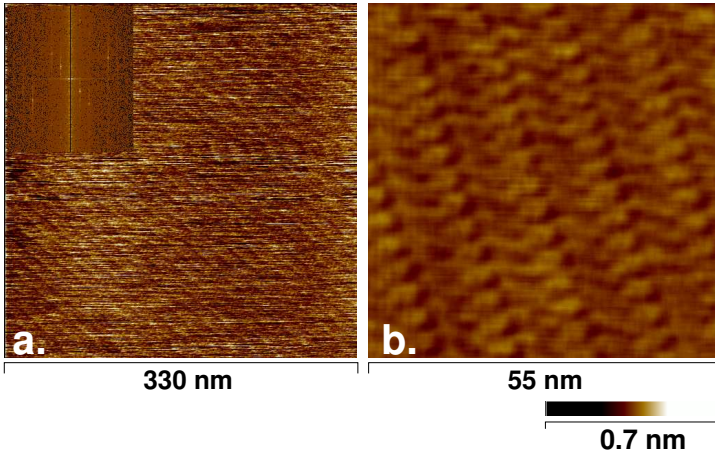


Figure 6.4: Topography showing a (110) face at high-resolution. (a), The image shows the topography at scan rate 88 nm/s of 512 scan lines. The measured height differences are less than 1 nm (color scale bar). Inset of (a), power spectral density plot shows significant peaks corresponding to periodicities of 3.74 and 11.5 nm. (b) Corresponding band pass filtered data (frequency bands around peaks corresponding to 3.74 and 11.5 nm and higher order were selected) reveals visibly a more detailed surface structure.

of a fluid cell allowed to run the experiments at conditions of crystal growth.

An image of the deflection signal is shown in fig. 6.1 The image shows a characteristic terrace like surface structure with diagonal running steps. Heights of single steps were determined from the corresponding topographical data (not shown). The major population of step heights on the (110) surface was found to be 5.5 ± 0.3 nm ($n=12$), which is of the order of single unit cells [8]. But different step heights can be clearly read from corresponding height profiles. A typical height profile is given in fig. 6.1b along the corresponding line given in fig. 6.1a Besides a major step height of about 5.5 nm also step heights of about 2.8 nm could be detected (see also green and blue arrow in fig. 6.1a) The corresponding step velocities differ not significantly. It is remarkable, that these small steps occurred pairwise, only. In some images, bunches of steps (macrosteps) dominated the total scan area (see arrow in inset of fig. 6.1), what is characteristic for large lysozyme crystals and crystals growing at high supersaturation [15]. The overall height of those macrosteps were measured to be multiples of 5.5 nm.

During image acquisition the crystallization conditions were maintained. Therefore image sequences could be recorded from the crystal surface which represent the time dependent change of the surface topology during crystal growth. The sequence of images (fig. 6.2) shows a characteristic double step moving from the upper left to the lower right of the image. Every scan took about 22 s. This procedure allowed to estimate step velocities with an average value of 24.4 ± 0.7 nm/s from 17 independently growing steps.

In order to calculate the rate of crystal growth in normal direction to the surface, 75 terrace widths were measured. The values range from

150 nm to over 1100 nm with an average of 473 ± 29 nm. A crude estimate of the normal growth rate (step height / step width \times step velocity) delivers a corresponding normal growth rate of 0.28 ± 0.03 nm/s.

In some image sequences events of two-dimensional nucleation could be observed. The heights of these newly formed terraces were equal to the growing terraces of 5.5 nm. Fig. 6.3 shows a newly formed two-dimensional islands (fig. 6.3a) on the (110) surface, which grows in lateral direction (fig. 6.3b) and fuses with growing neighboring terraces (fig. 6.3c). This finding resembles previous observations [3, 11, 12].

High-resolutions scans revealed the molecular packing of the (110) surface. To achieve molecular resolution, heights below 1 nm had to be resolved in z-direction. Fig. 6.4a shows the topography of the raw data with the corresponding spectral power density in the inset. Significant peaks corresponding to periodicities of 3.74 nm and 11.5 nm could be identified from the plot of spectral power density. These values agree with the results obtained by Li et al. [9] and represent the dimensions of the two dimensional unit cell of the (110) surface. The noise of the original topography could be reduced by filtering the data with a band pass. The results are given in fig. 6.4b which reveals the surface structure at molecular level.

6.3.2 Linescan of (101) surface at molecular resolution

Images of molecular resolution were acquired for the analysis of growing (101) surfaces of tetragonal lysozyme crystals. The lysozyme concentration was adjusted to 3% (w/v) for these experiments.

Fig. 6.5 shows the topography of the (101) surface with molecular resolution. The periodic surface topography had an amplitude of 4.2 nm (see below). Therefore a height resolution of about 1 nm was

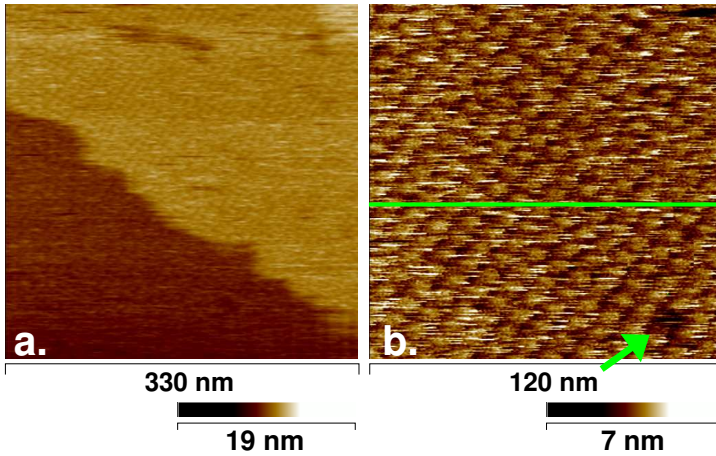


Figure 6.5: Topography of the (101) surface at different magnification. (a), topography of a (101) surface of $330 \times 330 \text{ nm}^2$ (scan rate 133 nm/s). The height differences are larger than 5 nm (color scale bar). Growing terraces can be identified easily. (b) High resolution topography of $120 \times 120 \text{ nm}^2$ showing single defects (see arrow), indicating that true resolution of the molecular lattice could be achieved. The green line indicates a scan line which was chosen for following images in linescan mode (see fig. 6.6b).

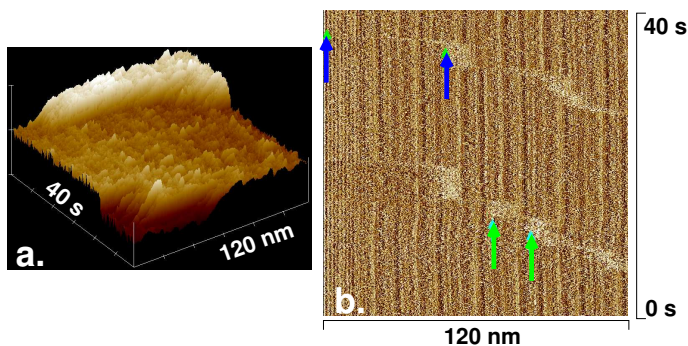


Figure 6.6: Linescan images obtained by scanning across a growth step on the (101) face. a, the image shows a linescan in three-dimensional presentation. The y-direction gives the time evolution of a discrete growth event on the (101) face of during scanning along the direction marked in green in fig. 6.5b. (b) Deflection data of another linescan image recorded as described in (a). Discrete growth events are marked by arrows. The periodic pattern of vertical lines corresponds to the feature of the molecular lattice of fig. 6.5b.

sufficient to image single unit cells of the periodic structure. Occasionally single defects of unit size could be observed in scans with high resolution.

Based on these data, images in linescan mode (s. *Materials and Methods*) were acquired, which allowed to monitor crystal growth in one direction on a molecular scale. The selected scan line is tagged as a green line in fig. 6.5. Fig. 6.6 shows the corresponding topographical (fig. 6.6a) as well as deflection data (fig. 6.6b) of images in linescan mode. In fig. 6.6b, periodic vertical lines are visible corresponding to the topographic features along the linescan as marked in fig. 6.5b. A significant influence of a lateral drift could be neglected for the following reasons. It can be read from fig. 6.6b, that the derived velocity of the step-like growth is at least one order of magnitude larger than observed for the lateral drift of linescan images (see Material and Methods) which occurs in a time independent monotonic fashion. It is conspicuous, that the boundary moves from the right to the left in a mercurial motion, as can be seen from the time evolution of the linescan signal (fig. 6.6b). 75 step lengths were measured. The average step length was 32.7 ± 2.7 nm. Between each step like motion there were dead times up to 4 s, where no boundary motion could be detected. The heights of the steps of the (101) face were measured to be 4.2 ± 1.2 nm.

6.4 Discussion

Bimolecular growth steps were observed on the (110) face of tetragonal lysozyme crystals [3, 7] which has been confirmed by high resolution studies by AFM [9]. From these studies it was suggested that the minimum repeating unit in that direction [14] consists of tetramers of

lysozyme with 4_3 axes parallel to the (110) crystal face (cf. [9]). For the width of the growth steps and growth units 5.6 nm and multiples of this value were reported. Our data confirm, as major height of growth steps a value of 5.5 nm which closely resembles the reported value. But in addition we occasionally observed growth steps of 2.8 nm which always appeared pairwise. Therefore we propose two packing arrangements for the (110) face, besides growth layer of at least bimolecular height, also those of monomolecular height. In terms of the helical tetramer growth unit [9] centered around the 4_3 crystallographic axis, this result would suggest the occurrence of a tetramer unit as well as an octamer unit for the (110) face. The formation of 2_1 helices had been suggested by Durbin & Feher, 1990 [3] and Nadarajah & Pusey, 1996 [14] while Li et al. [9] proposed the alternate arrangement by only 4_3 helices. Our data would indicate that both packing arrangements can occur in parallel for the (110) face. Due to the proposed orientation of the lysozyme molecules one expects a relatively smooth (110) face compared to that of the (101) face [10]. To add evidence for this proposal especially for the surface structure of the (101) face we analyzed the (110) face and the (101) face at molecular resolution. Comparison of the corresponding figures 6.4b and 5b. indicates heights for the unit cells of less than 1 nm at the (110) face and of about 4.2 nm at the (101) face. These findings are in line with the model of the proposed crystallographic structure [10]. Furthermore, we performed AFM linescan images to reveal the mechanism of growth on the (101) surface. AFM linescans have already been used as suitable procedure to obtain growth unit dimensions (cf. [8]) suggesting that the growth mechanism at the (110) surface occurs by the addition of lysozyme clusters formed in solution. Other investigators have proposed that lysozyme exists only in monomeric form

in solution [6, 13] and that the growth of lysozyme crystals should not be different to that of inorganic crystals [16, 17]. AFM linescan images (see fig. 6.6) across a growth step of the (101) face indicate discrete growth events of large two-dimensional size with diameters up to 90 nm and a stable height of about 4.2 nm which corresponds to the growth step height of the (101) face. The observed large diameter would rather indicate the attachment of lysozyme clusters of about ten tetramers in solution to the (101) face. If one considers the limited velocity of the linescan of about 1600 nm/s, it appears to be unlikely that within about 80 ms single lysozyme molecules in solution forming about ten tetramers become sequentially attached and aligned at the (101) face. Therefore we strongly suggest that the growth of tetragonal lysozyme crystals is dominated by addition of lysozyme clusters which were formed in solution or aggregated on the surface before reaching the incorporation site. However, the data do not strictly argue against the possibility that crystal growth occurs by direct insertion of monomers from solution. Further investigations are necessary to analyze the dimensions of inserted lysozyme clusters by scanning at higher scan rates in line scan mode in order to achieve time resolutions well below 10 ms.

6.5 Conclusion

In this study the molecularity of the growth step of the (110) face of the tetragonal lysozyme crystal was investigated by AFM. Besides the reported bimolecular step height [8] we also observed step heights of half of this size. The latter finding could be attributed to the appearance of monolayered-slices in addition to double-layered slices. The monolayered slices appeared pairwise. The surface of the correspond-

ing terraces should adopt the identical roughness, if the proposed crystallographic structure of the (110) face is correct. Further studies at the molecular level are necessary to give evidence for this suggestion. On the basis of the proposed structure [8] the height of the unit cells of the (110) face and (101) face should appear different in AFM images at molecular level. Comparison of the corresponding topographical images support the proposed crystallographic surface structure. Protein molecules have irregular geometries and lack strong ionic bonds in the corresponding crystals. Therefore, it is likely that large crystallization units occur randomly in the bulk solution. The growth of lysozyme crystals requires the transfer and attachment of such units from the bulk solution to the crystal surface. The derived large size of a growth unit from the analysis of the corresponding linescan image would support this mechanism of lysozyme crystal growth. But it cannot be excluded that lysozyme monomers attach to the surface and diffuse to the growth steps within a time scale far below the time resolution of a linescan.

References

- [1] Blake, C. C., R. H. Fenn, A. C. T. North, D. C. Phillips, and V. R. Sarma, 1966. On the conformation of the hen egg-white lysozyme molecule. *Proc. R. Soc. B* 167:378–388
- [2] Blake, C. C., D. F. Koenig, G. A. Mair, A. C. North, D. C. Phillips, and V. R. Sarma, 1965. Structure of hen egg-white lysozyme. A three-dimensional Fourier synthesis at 2 Angstrom resolution. *Nature* 206:757–61
- [3] Durbin, S. D. and W. E. Carlson, 1992. Lysozyme crystal-growth studied by atomic force microscopy. *J. Cryst. Growth* 122:71
- [4] Durbin, S. D., W. E. Carlson, and M. T. Saros., 1993. In-situ studies of protein crystal-growth by atomic-force microscopy. *J. Phys. D* 26:B128
- [5] Durbin, S. D. and G. Feher, 1990. Studies of crystal-growth mechanisms of proteins by electron-microscopy. *J. Mol. Biol.* 212:763
- [6] Gripon, C., L. Legrand, I. Rosenman, F. Boue, and C. Regnaut., 1998. Relation between the solubility and the effective solute-solute interaction for C-60 solutions and lysozyme solutions: a comparison using the sticky hard-sphere potential. *J. Cryst. Growth* 183:258

-
- [7] Konnert, J. H., P. d'Antonio, and K. B. Ward, 1994. Observation of growth steps, spiral dislocations and molecular packing on the surface of lysozyme crystals with the atomic force microscope. *Acta Cryst. D* 50:603
- [8] Li, H. Y., A. Nadarajah, and M. L. Pusey., 1999. Determining the molecular-growth mechanisms of protein crystal faces by atomic force microscopy. *Acta Cryst. D* 55:1036
- [9] Li, H. Y., M. A. Perozzo, J. H. Konnert, A. Nadarajah, and M. L. Pusey, 1999. Determining the molecular-packing arrangements on protein crystal faces by atomic force microscopy. *Acta Cryst. D* 55:1023
- [10] Li, M. R., A. Nadarajah, and M. L. Pusey., 1999. Growth of (101) faces of tetragonal lysozyme crystals: determination of the growth mechanism. *Acta Cryst. D* 55:1012
- [11] Malkin, A. J., Y. G. Kuznetsov, W. Glantz, and A. McPherson., 1996. Atomic force microscopy studies of surface morphology and growth kinetics in thaumatin crystallization. *J Phys. Chem.* 100:11736
- [12] Malkin, A. J., Y. G. Kuznetsov, and A. McPherson., 1996. Defect structure of macromolecular crystals. *J. Struct. Biol.* 117:124
- [13] Muschol, M. and F. Rosenberger., 1996. Lack of evidence for prenucleation aggregate formation in lysozyme crystal growth solutions. *J. Cryst. Growth* 167:738

-
- [14] Nadarajah, A. and M. L. Pusey., 1996. Growth mechanism and morphology of tetragonal lysozyme crystals. *Acta Cryst. D* 52:983
- [15] Vekilov, P. G., J. I. D. Alexander, and F. Rosenberger, 1996. Non-linear response of layer growth dynamics in the mixed kinetics-bulk-transport regime. *Phys. Rev. E* 54:6650
- [16] Vekilov, P. G., M. Ataka, and T. Katsura, 1993. Laser michelson interferometry investigation of protein crystal-growth. *J. Cryst. Growth* 130:317
- [17] Vekilov, P. G. and F. Rosenberger., 1996. Dependence of lysozyme growth kinetics on step sources and impurities. *J. Cryst. Growth* 158:540
- [18] Yip, C. M., M. L. Brader, M. R. DeFelippis, and M. D. Ward, 1998. Atomic force microscopy of crystalline insulins: The influence of sequence variation on crystallization and interfacial structure. *Biophys. J.* 74:2199

7 Structural Calorimetry of Main Transition of Supported DMPC Bilayers by Temperature Controlled AFM

O. Enders^α, A. Ngezahayo^α, M. Wiechmann^α, F. Leisten^α and
H.-A. Kolb^α

^α Institute of Biophysics, University Hannover, Herrenhäuser Str. 2, D-30419 Hannover, Germany

Biophysical Journal, accepted. Copyright 2004 Biophysical Society.

Abstract

Atomic force microscopy (AFM) at high temperature resolution ($\Delta T \lesssim 0.1$ K) provided a quantitative structural calorimetry of the transition from the fluid (L_α)- to the gel ($P_{\beta'}$)-phase of supported dimyristoylphosphatidylcholine (DMPC) bilayers. Besides a determination of the main transition temperature (T_0) and the van't Hoff transition enthalpy (ΔH_{vH}), the structural analysis in the nm-scale at T close to T_0 of the ripple phase allowed an experimental estimation of the area of cooperative units from small lipid domains. Thereby, the corresponding transition enthalpy (ΔH) of single molecules could be determined. The lipid organization and the corresponding parameters T_0 and ΔH_{vH} (ΔH) were modulated by heptanol or external Ca^{2+} and compared to physiological findings. The size of the cooperative unit was not significantly affected by the presence of 1 mM heptanol. The observed linear relationship of ΔH_{vH} and T_0 was discussed in terms of a change in heat capacity.

7.1 Introduction

It is well accepted that the specific lipid composition and their corresponding phase state in membranes play a crucial role for the activity of embedded membrane proteins. A prominent example represents the potassium channel KcsA [54, 57]. The question arises whether regulatory functions of specific agents on membrane proteins can be mediated by induced phase transitions of surrounding lipid domains rather than by binding to specific epitopes [8]. Support of this concept is given by the known dependence of protein kinase C on alcohol [46] or the finding that long chain alcohols like heptanol or octanol re-

versibly inhibit gap junctional coupling of neighboring cells [47, 51]. It could be proposed that the addition of hydrophobic components alter the phase state of lipid domains of the membrane which in turn could effect the functional properties of the embedded integral membrane proteins.

A large number of experimental and theoretical studies of thermally induced fluid-gel transitions in phospholipid bilayers have been carried out, using a variety of biophysical methods. A conceive compilation of thermodynamic properties of lipid phases can be found in Koynova and Caffrey [22] and the associated database LIPIDAT. As direct method to reveal the thermodynamic properties of phase transition scanning calorimetry is used, which allows the determination of phase transition temperatures and enthalpies [16, 26, 27]. Preferentially the main transition between gel phase and fluid phase has been elucidated. The gel phase is often subdivided into the $L_{\beta'}$ - and the $P_{\beta'}$ -phase, whereby the latter precedes the first, when the lipid system is cooled down from the fluid L_{α} -phase. The $P_{\beta'}$ -phase plays an emphasized role due to the regular surface pattern, which at first was described by Tardieu, Luzzati and Reman, 1973. This phase of the bilayer is characterized by a quasi-periodic undulation in one dimension which is called *ripple phase*. The phase was structurally investigated by electron microscopy preferentially using the freeze fracture technique [5, 33, 34, 55], x-ray diffraction using synchrotron radiation [6, 15, 20, 28, 29, 30, 31, 45, 48, 50, 52] or neutron scattering [35].

The $P_{\beta'}$ -phase is subdivided into two sub-states which differ in their wavelength and shape of ripples as well as in the dependence on the cooling or heating history [6, 14, 19, 31, 33, 45]. The two sub-states are denoted as Λ - and $\Lambda/2$ -ripples, because the ripple wavelength of both states differ by about a factor of two [42]. The structure of $\Lambda/2$ -

ripples was studied by x-ray diffraction techniques and scanning tunneling microscopy (STM) techniques. Electron density maps, which were calculated from x-ray diffraction data, indicate for $\Lambda/2$ -ripples a sawtooth-like shape [20, 33, 50, 56, 58], while the Λ -ripples show a symmetric profile [20]. More recently atomic force microscopy (AFM) was used to reveal information on the morphology of the $P_{\beta'}$ -phase of bilayers made of phosphatidylcholines [7, 19, 24, 37]. This approach allows to monitor structural changes of bilayers in buffered aqueous solutions close to real-time [2, 9, 13, 19, 21, 53].

In this paper the phase transition from the L_{α} - to $P_{\beta'}$ -phase of dimyristoylphosphatidylcholine (DMPC) is studied at high temperature resolution ($\Delta T \lesssim 0.1$ K) by AFM. The analysis of the topographies is performed at a lateral resolution in the nm-scale which allows a detailed study of the transition between Λ - and $\Lambda/2$ -ripples. Besides the main transition temperature (T_0), the van't Hoff transition enthalpy (ΔH_{vH}) is determined. For the first time the size of lipid molecules organized in cooperative units could be derived from a specific image analysis. With the knowledge of the cooperative unit the enthalpy of transition of single molecules could be calculated from the van't Hoff enthalpy. The modulatory effect of heptanol and by Ca^{2+} in the imaging buffer on the caloric parameters is analyzed and compared with physiological findings. For the observed dependence of ΔH_{vH} (ΔH) on T_0 a non-vanishing change in heat capacity is introduced and discussed.

7.2 Material and Methods

7.2.1 Sample preparation

Supported bilayers were prepared by a vesicle fusion method as described previously [21]. 1,2-dimyristoyl-rac-glycero-3-phosphocholine was purchased from Sigma, Germany and dissolved in chloroform (Roth, Karlsruhe, Germany). After removing the solvent by a rotary evaporator, the lipid was resuspended in buffer (5 mM K-HEPES at pH 7.2) at a concentration of 10 mg/ml. After dispersing the suspension by a vortex mixer VF2 (Janke & Kunkel, Staufen, Germany) and ultrasonification in a bath sonicator (Branson Ultrasonics 1200E3, Danbury, Connecticut, USA) for 30 min, the suspension was left at 4°C overnight. For the experiments the suspension was diluted 10-fold by an adsorption buffer (1 mM EDTA, 5 mM K-TRIS, pH 9). Freshly cleaved ruby muscovite mica (Mica corp., New York, USA) was glued to a sample holder and a drop of about 20 μl of the vesicle suspension was placed on the mica surface. The sample holder was placed in a sealed container together with a reservoir of water and incubated at 37°C for about 30 min. The sample was allowed to cool down to room temperature before removing the excess vesicle suspension. Without allowing the sample to dry the coated mica surface was flushed 3 to 5 times with the imaging buffer (50 mM KCl, 5 mM MgCl_2 , 5 mM K-HEPES, pH 7.2) and mounted to the atomic force microscope (Nanoscope IIIa, Multimode, Veeco Instruments, Mannheim, Germany).

7.2.2 Temperature controlled atomic force microscope

The atomic force microscope was modified as follows to adjust and to record on-line the temperature of the sample during image acquisition. The head module of the microscope, which houses the deflection detecting optics and electronics were equipped with low-cost peltier modules (Conrad Elektronik, Hirschau, Germany). The peltier modules were controlled by a LabView System (National Instruments, Austin, Texas, USA). To avoid thermal drifts, the driving signal of the peltier devices was generated by a closed-loop continuous software PI-controller whereby the error signal was delivered from a surface temperature sensor glued to the head module. The hot side of each peltier device was connected to an aluminum block with a cylindrical cranial open chamber which was filled with water. In each cooling chamber a bar from copper was immersed in a way that the walls were not in contact with the bar. The two bars were fixed with a tripod and connected to an aluminum block, which was placed in an ice cooled container. In this way the temperature of the hot side of the peltier devices was kept at sufficient low temperatures while substantial mechanical noise was avoided.

The sample temperature was monitored by a digital thermometer GMH 3230 (Greisinger, Regenstauf, Germany) equipped with a coated miniature probe (physitemp IT23, Clifton, New Jersey). Because the viton-seal of the commercial fluid cell was not used, the small temperature probe could be placed directly into the fluid cell in close proximity of the sample surface and in direct contact to the imaging buffer.

7.2.3 Image acquisition and processing

All images were acquired in contact mode using Silicon-Nitride Olympus OMCL-PSA 400 tips with a spring constant of 0.02 N/m (Olympus co., Tokyo, Japan) at a scan rate of about 6 lines/s at minimal loading force. After adjusting the temperature to a new value the setup was allowed to equilibrate for about 5 to 10 minutes until the thermal drift was well below 0.1 K/min. The topographies were post processed by a home made software and the filmgimp image processing system (motion picture studios, Hollywood, California). After adding the calibrated error signal images to the topographies, to produce more accurate topographies [11], which are in first order independent on the actual settings of the feedback circuit of the microscope and the scanning speed, each scan line was flattened by subtracting the result of a polynomial fit up to 3rd order. In general, only those samples were considered for this fit, which corresponded to non-elevated domains in the topographies. To remove high frequency noise, the topographies were processed by a Gaussian spatial filter ($\sigma = 1.5$ or 3 pixel, 21x21 matrix).

Height histograms were calculated using filmgimp. For further description of image analysis see Results.

To determine the size of the cooperative unit, a correlation difference image of two consecutive scans was needed (see Results). The drift vector between the two images in the xy-plane was calculated by determination of the global maximum of the correlation coefficient function of the two topographical or deflection maps. The difference image was produced by subtracting the second topography from the first one, corrected by the drift vector. The correlation procedure is necessary to compensate for lateral drifts of the scanner, which can be

caused by time dependent temperature gradients. The derived image is called correlation difference image.

3D-rendering of images was performed using the software package dxopen (IBM). Data are given as mean \pm SD.

7.3 Results

7.3.1 Topography of supported DMPC bilayers in the fluid-crystalline and gel-phase

The topography of mica supported DMPC bilayers is analyzed in aqueous solution as function of temperature in contact mode. The imaging is started at temperatures above the main phase transition of DMPC. At these temperatures the bilayer exhibits a smooth surface without defects within the height of a DMPC bilayer of about 4.8 nm. A representative image is shown in fig. 7.1 *a*. In the figure, which was recorded at 302.6 K, the membrane surface exhibits an irregular corrugated topography with height differences (peak to bottom) below about 0.2 nm. At this temperature the DMPC bilayer can be considered to be in the fluid-crystalline- or L_α -phase [22]. The defect-free surface allows repeated scans of the same area without significant contamination of the tip. Before a detailed analysis for the step-wise change of topography during the transition from the fluid-crystalline- to the gel-phase is presented and analyzed, the topography of DMPC at low temperature ($T = 295.5$ K) is shown in fig. 7.1 *b* and at higher magnification in fig. 7.1 *c*. The bilayer surface exhibits the typical ripple structure. This characteristic structure can be attributed to the gel- or $P_{\beta'}$ -phase. The height difference (peak to bottom) is about 0.3 nm. The ripples run almost equidistant and form regular domains

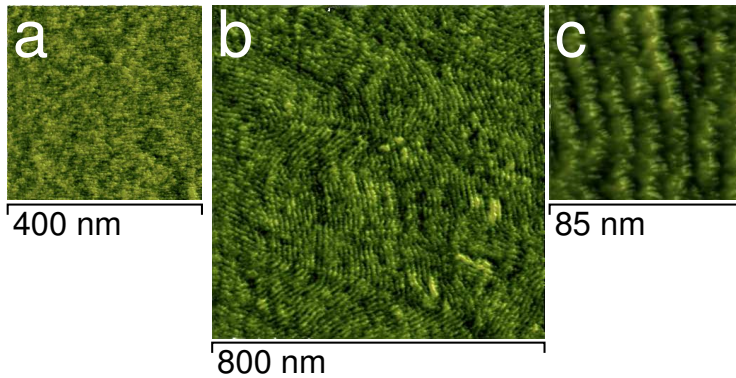


Figure 7.1: Topography of a supported DMPC bilayer in fluid- (L_α) and gel-phase ($P_{\beta'}$). *a*, topography in L_α -phase at 302.6 K well above the main transition. *b* and *c*, DMPC bilayer surface recorded at 295.5 K at different magnification. In *a* the surface appears smooth with an undulating pattern of a height below 0.2 nm. Ripples in image *b* and *c* are ordered and have a peak to bottom value of at least 0.3 nm. The mean distance between neighboring ripples is about 12 nm. 256 lines per image were scanned with 512 samples per line.

of 10 to 30 ripples in parallel to each other. From the corresponding Fourier transform of such domains a periodicity of 12.3 ± 0.3 nm is obtained. If a change in direction of the ripples is observed, it occurs predominantly at an angle of $118 \pm 9^\circ$.

7.3.2 Topography at temperatures of main transition

The image records are started at a temperature above the main transition from the L_α - to the $P_{\beta'}$ -phase. The temperature is lowered stepwise and the bilayer surface is imaged respectively. Fig. 7.2 shows four representative images at temperatures of 297.0 K to 296.1 K, which are within the temperature range of main transition. At the onset of main transition at 297.0 K (fig. 7.2 *a*) the first ripples emerge out of the smooth bilayer surface, which are characteristic for the gel phase (compare fig. 7.1 *b*). At a lower temperature, 296.7 K (fig. 7.2 *b*), the ripple density increases visibly, until the surface becomes almost completely covered by ripples at 296.3 K (fig. 7.2 *c*). Cooling the sample further by 0.2 K to 296.1 K causes a sudden and significant change of density and profile of ripples (fig. 7.2 *d*). The ripples are closer to each other and the periodicity of the ripples reflects now those already shown in fig. 7.1 *b*. The profiles of the ripples are given in the insets of fig. 7.2 *c* and 7.2 *d*. As can be read from the insets, the corresponding wavelength is reduced by a factor of two which can be attributed to a change from the Λ -ripples to the $\Lambda/2$ -ripples [42]. Also the height of the ripples appears to be significantly reduced. But for the reliability of this change it should be considered that the access of the tip to image the depressions in the nm-scale might be limited by the finite radius of the scanning tip which is of about the same order of magnitude.

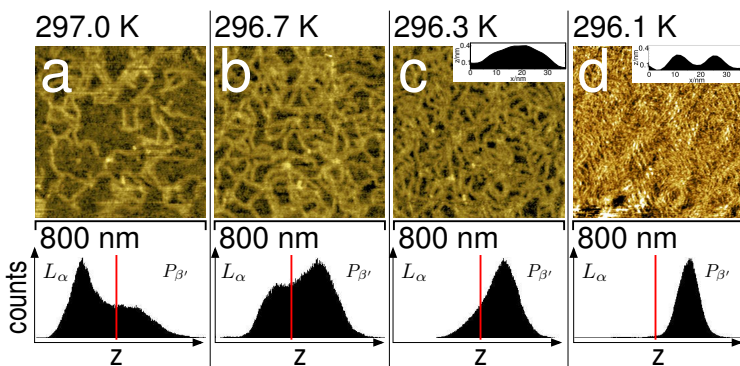


Figure 7.2: Topography of a DMPC bilayer at decreasing temperatures as indicated in *a*, *b*, *c*, *d* and the corresponding frequency histograms of height z (lower row). Comparison of *c* and *d* shows a transition from Λ - to $\Lambda/2$ -ripples which is reflected in the corresponding ripple profiles (insets of *c* and *d*). The blue line in the frequency histograms indicates the threshold which separates the heights of the L_{α} - and $P_{\beta'}$ -phases. For further explanation see text. Each image consists of 512×256 pixel.

7.3.3 Structural calorimetry of main transition by image analysis

From the acquired images the fraction of the scanned area presenting the $P_{\beta'}$ -state of the bilayer ($f_{P_{\beta'}}$) can be estimated. The frequency histogram of heights of the image is calculated, and a suitable threshold of the lower height level is selected to separate the smooth bilayer of the L_{α} -phase from the ripple structure of the $P_{\beta'}$ -phase. Fig. 7.3 shows an example of this image analysis. The blue colored area represents the L_{α} -phase. The corresponding threshold is drawn as vertical line in the height histogram (inset). The integral of histogram below this threshold reflects the area of L_{α} -phase, while the integral of the height histogram above the threshold corresponds to the area of bilayer in the $P_{\beta'}$ -phase. The latter value divided by the total integral yields the fraction $f_{P_{\beta'}}$. Because a high resolution is applied which allows to identify individual ripples also the intermediate heights along their profile contribute to the height histogram. Thereby, the height distributions appear to be widened and in many cases two separate Gaussian-like distributions cannot be easily discriminated especially for temperatures below the main transition (compare height distributions in fig. 7.2). The derived relation $f_{P_{\beta'}}$ as function of temperature is given in fig. 7.4. The data points, especially in the range of main transition, present the mean value of up to three analyzed images at about the same temperature within a resolution of 0.1 K.

For a theoretical description of main transition the two phases are assumed to be in thermodynamic equilibrium at the applied temperature.

If K is the equilibrium constant of the phase transition between the two phases:



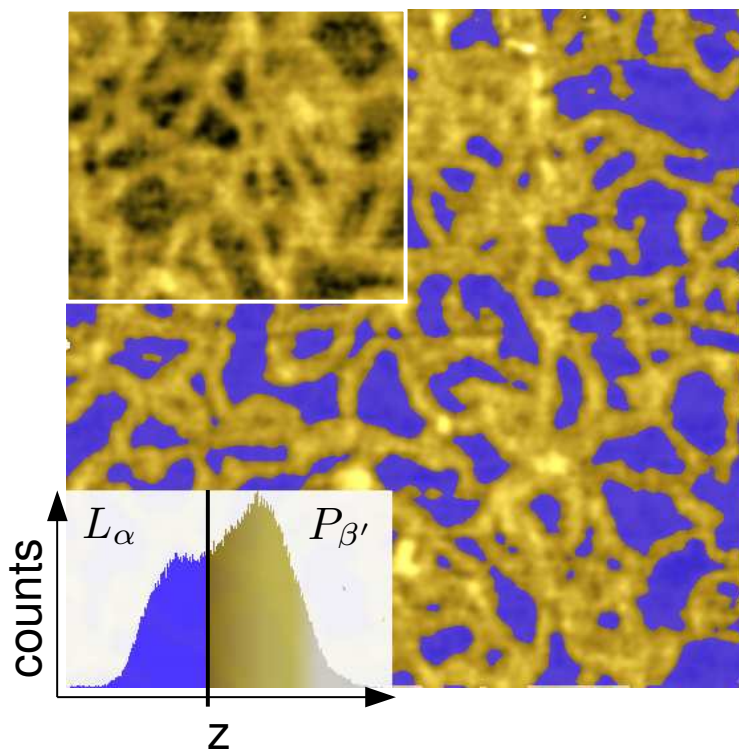


Figure 7.3: Post-processing of a topography of a supported DMPC bilayer. The image shows the bilayer at a temperature slightly below the main transition. After selecting a suitable height threshold separating the L_{α} - and $P_{\beta'}$ -phase, the area which corresponds to the L_{α} -phase, is colored blue. The inset shows the corresponding frequency histogram of heights z . The blue part corresponds to the values below the threshold. The values corresponding to the $P_{\beta'}$ -phase are given by golden colors.

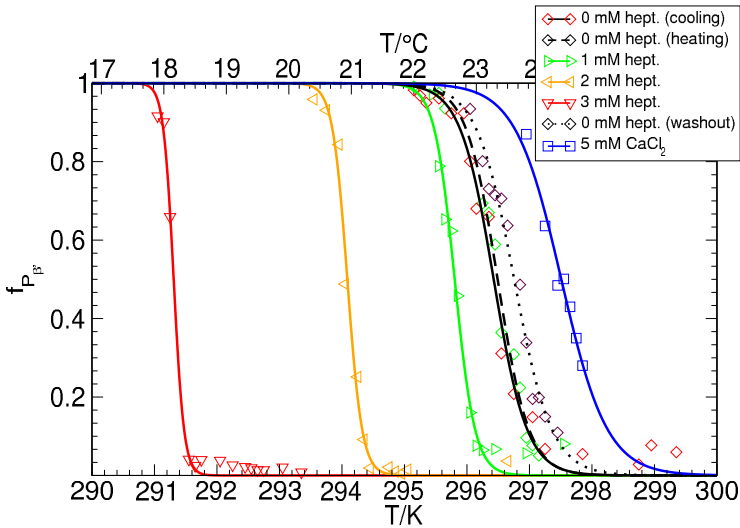


Figure 7.4: Fraction of $P_{\beta'}$ -phase ($f_{P_{\beta'}}$) as function of temperature T .

The data were recorded consecutively at increasing concentrations of heptanol and after washout, as indicated. In general, the data were derived by changing T in cooling direction. For the data denoted as 0 mM hept. (heating) the temperature direction was reversed at the lowest value of T . Thereafter 5 mM $MgCl_2$ was replaced by 5 mM $CaCl_2$ in the imaging buffer. The drawn curves represent a fit of eq. 7.4 to the data. The corresponding values of T_0 and ΔH_{vH} are included in tab. 7.1. For further details see text.

it can be described by the relation:

$$K = \frac{f_{P_{\beta'}}}{1 - f_{P_{\beta'}}} \quad (7.2)$$

According to [27] K can be described as function of T by the integrated form of the van't Hoff equation:

$$\ln K = \frac{\Delta H_{vH}}{R} \left(\frac{1}{T_0} - \frac{1}{T} \right) \quad (7.3)$$

ΔH_{vH} represents the van't Hoff transition enthalpy, R the gas constant and T_0 the temperature at $K = 1$, where half of the bilayer is in $P_{\beta'}$ -phase. T_0 is defined as the temperature of main transition. It should be noticed that in Eq. 7.3 the influence of a change of heat capacity at the transition is neglected (see Discussion). From Eq. 7.2 and 7.3 $f_{P_{\beta'}}$ can be expressed as function of T :

$$f_{P_{\beta'}} = \frac{1}{1 + \exp\left(\frac{\Delta H_{vH}}{R} \left(\frac{1}{T} - \frac{1}{T_0}\right)\right)} \quad (7.4)$$

Eq. 7.4 was used to describe the experimental data of fig. 7.4, which yields as result T_0 and ΔH_{vH} . The corresponding values are included in table 7.1.

7.3.4 Phase transition of DMPC bilayer in the presence of heptanol or Ca^{2+}

The phase transition of a DMPC bilayer was analyzed after addition of the long chain alcohol heptanol at different concentration to the imaging buffer. For these experiments the heptanol-free imaging buffer was subsequently replaced by solutions containing 1 mM, 2 mM and 3 mM

heptanol. Without changing the tip or sample the phase transition was monitored starting at temperatures above the main transition, respectively. The corresponding relationship $f_{P_{\beta'}}$ versus temperature is included in fig. 7.4. From a description of $f_{P_{\beta'}}$ versus T by Eq. 7.4 the values of T_0 and ΔH_{vH} could be determined (table 7.1). With increasing heptanol concentration T_0 decreases and ΔH_{vH} increases.

It can be read from fig. 7.4, that the temperature width of phase transition decreases with increasing heptanol concentration. Therefore, within the limit of temperature resolution of about 0.1 K a comparison of fig. 7.5 *a* and *d* as well as of fig. 7.5 *b* and *e* shows that a transition from the Λ - to the $\Lambda/2$ -ripples can be discriminated at lower heptanol concentration. The height of Λ -ripples decreased with increasing heptanol concentration (0 mM heptanol: 0.30 ± 0.05 nm (N=21), 1 mM heptanol: 0.27 ± 0.05 nm (N=9) and 2 mM heptanol: 0.18 ± 0.02 nm (N=15)). But at 3 mM heptanol the phase transition is completed within a small temperature interval of about 0.4 K, which did not allow a discrimination between Λ - and $\Lambda/2$ -ripples. Fig. 7.5 *c* is recorded at 3 mM heptanol and 291.6 K and shows the L_{α} -phase and a few ripple-like structures. At 291.3 K the total area is already covered by $\Lambda/2$ -ripples (fig. 7.5 *f*). After washout of 3 mM heptanol the recorded phase transition (fig. 7.4) closely resembles the behavior of the heptanol-free DMPC bilayer which can be seen from the derived values of T_0 and ΔH_{vH} (table 7.1). This finding indicates an almost reversible effect of heptanol on the main transition.

Besides a modification of the bilayer by heptanol, the water-bilayer interface was affected by replacing 5 mM MgCl_2 in the imaging buffer by 5 mM CaCl_2 , which yielded a free Ca^{2+} -concentration of 4 mM. The corresponding data are included in fig. 7.4 and table 7.1. The analysis of phase transition shows that T_0 increases by about 0.8 K

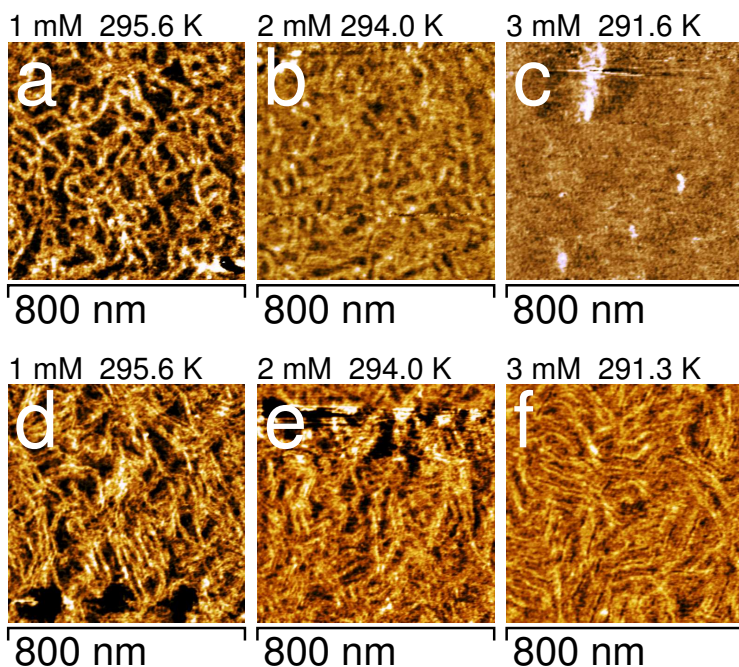


Figure 7.5: Topographies of a DMPC bilayer at heptanol concentrations of 1 mM (*a* and *d*), 2 mM (*b* and *e*) and 3 mM (*c* and *f*). The pairs of images were consecutively scanned. The upper row of images (*a*, *b* and *c*) shows the bilayer with Λ -ripples. *d*, *e* and *f* shows the corresponding images which were recorded thereafter at lower temperatures ($\Delta T \lesssim 0.1$ K). The pattern of the topography changed to $\Lambda/2$ -ripples. At 3 mM heptanol (*c* and *f*) the phase transition from L_{α^-} to $P_{\beta'}$ -phase is completed within $\Delta T = 0.3$ K.

and ΔH_{vH} decreases significantly as compared to the control. Because the temperature width of phase transition increased by the presence of Ca^{2+} (fig. 7.4), Λ - and $\Lambda/2$ -ripples could be discriminated (data not shown).

7.3.5 Cooperative unit n_c

It is known that the derivation of ΔH_{vH} strongly depends on the average number of interacting lipid molecules which simultaneously transit from the L_α -phase to the $P_{\beta'}$ -phase [16]. This number is noted as cooperative unit n_c . By correlation analysis n_c could be determined from pairs of consecutive images. The images (7.6 a, b) were obtained at a time difference of about 3 min and a temperature decrease of $\Delta T \lesssim 0.2$ K. Using a correlation algorithm to take into account a possible drift of the position of the scanned area in respect to the tip, the two images could be subtracted from each other. Fig. 7.6 c shows as result elevated domains of newly emerged ripples and deeper domains corresponding to ripples which disappeared as well as unchanged lipid areas of intermediate height. For clearer presentation fig. 7.6 d shows the newly emerged ripples and domains wherein ripples disappeared at different color. The two types of domains, those of emerged ripples and of domains wherein ripples disappeared, had a mean area of $239 \pm 103 \text{ nm}^2$ and $117 \pm 19 \text{ nm}^2$, respectively. Assuming an average interfacial area of 0.6 nm^2 per lipid molecule of the bilayer [23, 40] cooperative units of 398 ± 172 and 195 ± 32 molecules were obtained, respectively. The two values are comparable within the experimental error. The mean area, number of molecules n_c and the standard deviations of the two domains were calculated using the result of six difference images derived in the absence and presence of 1 mM hep-

additives to imaging buffer	T_0	ΔH_{vH}	ΔH
	K	kJ mol^{-1}	kJ mol^{-1}
0 mM heptanol	296.5	-2928	-15.0
1 mM heptanol	295.8	-4487	-23.0
2 mM heptanol	294.1	-6087	-31.2
3 mM heptanol	291.3	-8570	-44.0
0 mM hept., washout	296.7	-2439	-12.5
5 mM CaCl_2	297.5	-2004	-10.3

Table 7.1: Main transition temperature (T_0) and enthalpy (ΔH , ΔH_{vH}). T_0 and ΔH_{vH} were derived from a fit of the data given in fig. 7.4 by eq. 7.4 using a cooperative unit $n_c = 195$ molecules (see text). ΔH of single molecules was calculated by eq. 7.5.

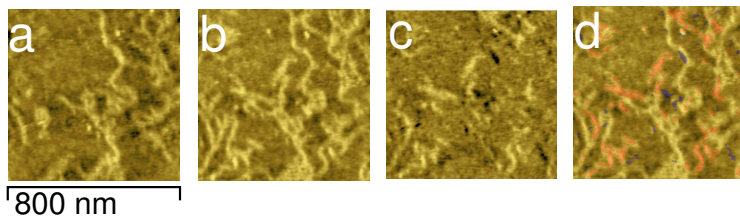


Figure 7.6: Determination of molecules (n_c) in a cooperative unit. a and b are two consecutively scanned images of the bilayer at two temperatures below T_0 . a was recorded at $|T - T_0| = 0.3$ K and b was recorded at decreased temperature of $\Delta T \lesssim 0.2$ K. After correction for a drift of the scanned area (see Materials and Methods) the difference of image a and b was calculated. The result is shown in c . The domains in d above suitably chosen height levels (threshold), the emerged ripples, are colored red and domains which are below the corresponding threshold are colored blue (domains wherein ripples disappeared). For clearer presentation the colored domains are superimposed with b and the result is shown in d . The topographies consist of 256 scan lines at 512 samples per line.

tanol. The size of the cooperative unit was not significantly affected by the presence of heptanol. The average number of domains per difference image was 164 for emerged domains and 119 for domains, wherein ripples disappeared.

Using the value of $n_c = 195$ molecules (see Discussion), the transition enthalpy of single lipid molecules ΔH could be calculated according to [16]:

$$\Delta H = \frac{\Delta H_{vH}}{n_c} \quad (7.5)$$

The corresponding values of ΔH are included in table 7.1.

7.4 Discussion

A temperature-controlled atomic force microscope allows to monitor the different states of phase transition in lipid bilayers [19, 53]. We developed a modified atomic force microscope with a temperature control of high accuracy ($\Delta T \lesssim 0.1$ K), which was applied at a lateral resolution in the nm-range for image analysis of mica supported DMPC bilayers. Besides the transition temperature (T_0), the van't Hoff transition enthalpy (H_{vH}) and the as yet theoretically introduced cooperative unit could be derived from structural data. In addition, the analysis is applied to reveal the effect of the incorporation of the long chain alcohol heptanol on the main transition. Heptanol was used to elucidate the mechanism of electrical uncoupling of gap junctions by long chain alcohols (c.f. [47]). The results are compared with the effect of Ca^{2+} binding to the bilayer-water interface.

7.4.1 Structural properties of ripple phase

To prepare defect free smooth DMPC-bilayer surfaces, the image analysis was started above T_0 in the L_α -phase. Cooling to temperatures below T_0 (figs 7.2) exhibited the characteristic topography of ripples as well as the transition from Λ - to $\Lambda/2$ -ripples of $P_{\beta'}$ -phase. Because unilamellar supported bilayers do not exhibit a ripple like topography [12, 24], we suppose that the applied vesicle fusion method yields defect-free multilamellar bilayers. The observed $\Lambda/2$ -ripple structure is characterized by a wavelength of 12.3 nm which is in reasonable agreement with the results of STM (10.7 nm) [58], transmission electron microscopy (11 nm) [58], x-ray diffraction (12 nm) [17, 18] or 14.3 nm [56] and AFM (12.5 nm) [24]. The observed change of direction of ripple structures by about 118° is comparable to the results of Mou et al. [37].

The observed ripple amplitude of about 0.3 nm is comparable with a value of 0.2 nm as derived from electron density maps [44], but application of STM yielded 2.4 nm [58].

7.4.2 Structure of the bilayer at main transition

An important structural feature of the transition from the L_α - to $P_{\beta'}$ -phase is the gradual appearance of ripples if the bilayer is cooled down (fig. 7.2). The ripples are not as ordered as reported in Kaasgaard et al. [19], Leidy et al. [24]. However it has to be taken into account, that the main transition is passed in cooling direction in our experiments. Cooling the sample to a temperature of 296.2 K leads to a sudden change of the morphology from Λ - to $\Lambda/2$ -ripples (see also fig. 7.1 b). The profiles of the two ripple morphologies (fig. 7.2) exhibit that the width of $\Lambda/2$ -ripples is about half the width of Λ -ripples

and that the height of $\Lambda/2$ -ripples is significantly reduced. This is in accordance with the results of Kaasgaard et al. [19].

If the sample is heated again, the $\Lambda/2$ -ripples melt directly into L_α -phase without converting to Λ -ripples (data not shown) (compare Cunningham et al. [6], Hatta et al. [14], Kaasgaard et al. [19], Matuoka et al. [31], Meyer [33], Sengupta et al. [45]). The data indicate that Λ -ripples are generated during the cooling process, only.

7.4.3 Structural calorimetry and estimation of the cooperative unit n_c

For the performed structural calorimetry it can be assumed that the sample in fluid is close to thermodynamic equilibrium, because the integral temperature rate was well below 0.1 K/min [27].

The image analysis is based on the derivation of suitable frequency histograms of heights as introduced by Tokumasu et al. [53]. Tokumasu et al. analyzed supported unilamellar DMPC-patches by an atomic force microscope at μm -scale, which was placed in a temperature controlled chamber. In the present experiments the upper surface of multilamellar bilayer was analyzed at nm-resolution and the image analysis was focused to T close to T_0 .

The obtained value of $T_0 = 296.5$ K (fig. 7.4, tab. 7.1) for DMPC-bilayers is in suitable agreement with values derived from differential scanning calorimetry [22]. The van't Hoff transition enthalpy ΔH_{vH} of about 2500 kJ/mol could be determined from fig. 7.5 as well. By use of differential scanning calorimetry values of 35650 ± 2400 kJ/mol [49], 7456 kJ/mol [27] and 5240 ± 1200 kJ/mol [16] were reported. But differential scanning calorimetry is applied to vesicle suspensions while for image analysis supported planar bilayers are used. It is known that the vesicle diameter also influences the enthalpy of phase

transition. Such an influence has been proposed from measurements of the heat capacity [38]. Therefore it appears to be likely that the different values of ΔH_{vH} could be related to the different geometry of the lipid system under investigation. As reliable value of the transition enthalpy those for single molecules (ΔH) was determined which is based on the knowledge of the cooperative unit n_c .

The number of interacting molecules contributing to n_c was estimated from structural data at the temperature range of phase transition. The data were obtained from the differences of pairs of consecutive images (fig. 7.6), recorded at about the same temperature (see below). The representative fig. 7.6 indicates, that the molecules of a cooperative unit are organized in small lipid domains. For the two types of domains, those of emerged ripples and of domains wherein ripples disappeared, cooperative units of 398 ± 172 and 195 ± 32 molecules were obtained, respectively. The larger mean value of n_c for emerged ripples could be caused by the fact that the phase transition (eq. 7.1) of the bilayer is not analyzed at true equilibrium. Probably, due to the ongoing cooling process of less than 0.1 K/min the equilibrium is shifted to the $P_{\beta'}$ -phase. Such a shift could cause the observed higher density of domains appearing in the $P_{\beta'}$ -phase than disappearing from L_{α} -phase yielding virtually larger domains for the $P_{\beta'}$ -phase. According to this consideration, a value of $n_c = 195$ molecules is assumed for the further. A possible dependence of n_c on temperature and/or the phase state cannot be excluded. n_c is of the same order of magnitude as theoretically derived (100 ± 50 ; 330; 1720 ± 120 [16, 27, 49]). Using eq. 7.5 a transition enthalpy for single molecules of $\Delta H = 15.0$ kJ/mol is obtained. This value is lower than the average value $\Delta H = 25.1 \pm 10.1$ kJ/mol as mainly determined

by differential scanning calorimetry [22], but comparable within the standard deviation.

7.4.4 Effect of heptanol and Ca^{2+} on main transition

At increasing concentration heptanol shifts T_0 to lower values (tab. 7.1). This is in accordance with observations, that alcohols and alkanes [32] of lower chain length, compared to the acyl chain of lipid, reduces T_0 [10, 25]. A heptanol mediated structural change by interdigitation can be ruled out at these low concentrations [41]. Furthermore, interdigitation should lead to a significant reduction in membrane thickness for the gel phase [36], which was not observed in the experiments.

It is proposed that a decrease in T_0 is responsible for the known regulatory influence of heptanol on the gating of gap junctional coupling. This assumption is supported by the observation that gap junctional coupling is blocked by heptanol or octanol concentrations as low as 1 mM [47, 51]. At this concentration T_0 is reduced by approximately 0.7 K (table 7.1). Furthermore, the washout of heptanol leads to values of T_0 and ΔH_{vH} as observed in the absence of heptanol (table 7.1). This reversibility is consistent with electro physiological results, which show that heptanol or octanol induced gap junctional uncoupling is reversible in the minute range [47, 51]. Therefore it is proposed, that heptanol fluidizes the lipid bilayer adjacent to the head-to-head associated cell-to-cell channels of neighboring cells forming the gap junctional coupling. The observed fluidization of the lipid bilayers could cause closure of the cell-to-cell channels of gap junctions.

After replacement of Mg^{2+} by Ca^{2+} in the imaging buffer an opposite effect is observed on the shift of T_0 , which is in agreement with

earlier results [3, 49]. It has been reported that divalent cations Ca^{2+} -ions and Mg^{2+} -ions bind to the membrane surface of negatively charged and neutral lipids like DMPC, changing the surface potential [1], the head group orientation [43] and the dipole potential [4]. Thereby, Ca^{2+} modifies the hydration shell of the head group region of the bilayer more effectively according to the Hofmeister series [3]. This might explain, why Ca^{2+} -ions shift the phase transition temperature compared to Mg^{2+} -ions.

7.4.5 Dependence of ΔH on T_0

The transition enthalpies ΔH and ΔH_{vH} show a significant dependence on the concentration of heptanol and on the presence of Ca^{2+} -ions. Ca^{2+} leads to a decrease of ΔH (increase of T_0), while heptanol increases ΔH (decrease of T_0 , fig. 7.7).

To explain the observed dependence of transition enthalpy on T_0 a possible change of heat capacity ΔC_p at the transition from L_α - to $P_{\beta'}$ -phase is considered. According to eq. 1 in Naghibi et al. [39] and taking into account the number of molecules n_c in a cooperative unit as well as using eq. 7.5, eq. 7.3 can be expressed as

$$\ln K = \frac{n_c(\Delta H_0 - T_0 \Delta C_p)}{R} \left(\frac{1}{T_0} - \frac{1}{T} \right) + \frac{\Delta C_p}{R} \ln \frac{T}{T_0} \quad (7.6)$$

ΔH_0 represents the transition enthalpy at 0 K. At T close to T_0 the last term can be neglected in a first approximation. Eq. 7.6 and eq. 7.5 indicate that ΔH depends linearly on T_0 due to a non-vanishing value of ΔC_p . If eq. 7.6 is applied to the data of fig. 7.7, $\Delta C_p = 5.6 \pm 0.4 \text{ kJ}/(\text{mol K})$ is derived. It is proposed, that a change of ΔH_{vH} (ΔH) by heptanol and Ca^{2+} -ions is a consequence of a non-

vanishing value of ΔC_p and a shift of T_0 . A similar relationship of transition enthalpy and transition temperatures with slopes of the same order can be derived from tab. 1 in Sturtevant [49] or the inset of fig. 1 in Mabrey and Sturtevant [27]), but a contribution of ΔC_p at the main transition was not considered.

7.5 Acknowledgment

We gratefully acknowledge support from the “Forschungsfond” of the University Hannover.

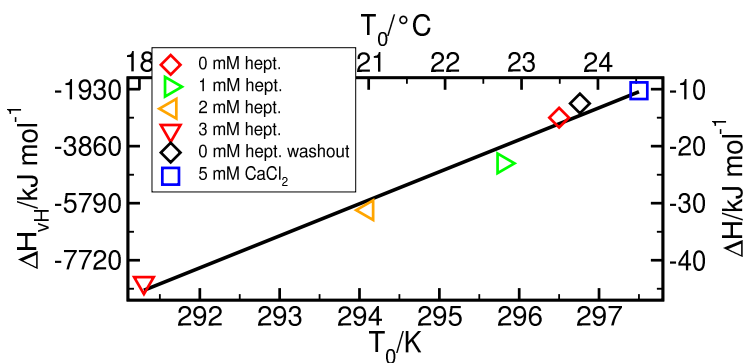


Figure 7.7: Transition enthalpy (ΔH) and van't Hoff transition enthalpy (H_{vH}) as function of T_0 . ΔH , H_{vH} and T_0 are given in table 7.1. For further explanation see Discussion.

References

- [1] Altenbach, C. and J. Seelig, 1984. Ca^{2+} binding to phosphatidylcholine bilayers as studied by deuterium magnetic resonance. Evidence for the formation of a Ca^{2+} complex with two phospholipid molecules. *Biochemistry* 23:3913–3920
- [2] Beckmann, M., P. Nollert, and H. A. Kolb, 1998. Manipulation and molecular resolution of a phosphatidylcholine-supported planar bilayer by atomic force microscopy. *J Membr Biol.* 161:227–233
- [3] Chapman, D., W. E. Peel, B. Kingston, and T. H. Lilley, 1977. Lipid phase transitions in model biomembranes. The effect of ions on phosphatidylcholines. *Biochim. Biophys. Acta* 464:260–275
- [4] Clarke, R. J. and C. Lüpfer, 1999. Influence of anions and cations on the dipole potential of phosphatidylcholine vesicles: A basis for the Hofmeister effect. *Biophys. J.* 76:2614–2624
- [5] Copeland, B. R. and H. M. McConnell, 1980. The rippled structure in bilayer membranes of phosphatidylcholine and binary mixtures of phosphatidylcholine and cholesterol. *Biochim. Biophys. Acta* 599:95–109
- [6] Cunningham, B. A., A. Brown, D. H. Wolfe, W. P. Williams, and A. Brain, 1998. Ripple phase formation in phosphatidylcholine:

- Effects of acyl chain relative length, position and unsaturation. *Phys. Rev. E* 58:3662–72
- [7] Czajkowsky, D. M., C. Huang, and Z. Shao, 1995. Ripple phase in asymmetric unilamellar bilayers with saturated and unsaturated phospholipids. *Biochemistry* 34:12501–5
- [8] de Kruijff, B., 1997. Biomembranes. Lipids beyond the bilayer. *Nature* 386:129–131
- [9] Dufrene, Y. F. and G. U. Lee, 2000. Advances in the characterization of supported lipid films with the atomic force microscope. *Biochim. Biophys. Acta* 1509:14–41
- [10] Elias, A. W., D. Chapman, and D. F. Ewing, 1976. Effects of n-alcohols, n-monocarboxylic acids, phenyl alkyl alcohols and quaternary ammonium compounds. *Biochim. Biophys. Acta* 448:220–230
- [11] Enders, O., E. Martinoia, C. Zeilinger, and H.-A. Kolb, 2001. Identification of membrane proteins imaged by atomic force microscopy using a template matching algorithm. *Chinese Physics* 10S:100–108
- [12] Fang, Y. and J. Yang, 1996. Role of the bilayer-bilayer interaction on the ripple structure of supported bilayers in solution. *J. Phys. Chem.* 100:15614–15619
- [13] Giocondi, M.-C., L. Pacheco, P. E. Milhiet, and C. L. Grmellec, 2001. Temperature dependence of the topology of supported dimirystoyl-distearoyl phosphatidylcholine bilayers. *Ultramicroscopy* 86:151–157

-
- [14] Hatta, I., S. Matuoka, M. A. Singer, and L. Finegold, 1994. A new liquid crystalline phase in phosphatidylcholine bilayers as studied by X-ray diffraction. *Chem. Phys. Lipids* 69:129–136
- [15] Hentschel, M. P. and F. Rustichelli, 1991. Structure of the ripple phase $P_{\beta'}$ in hydrated phosphatidylcholine multimembranes. *Phys. Rev. Lett.* 66:903–906
- [16] Hinz, H. J., 1972. Calorimetric studies of dilute aqueous suspensions of bilayers formed from synthetic L- α -lecithins. *J. Biol. Chem.* 247:6071–6075
- [17] Janiak, M. J., D. M. Small, and G. G. Shipley, 1976. Nature of thermal pretransition of synthetic phospholipids: Dimyristoyl- and dipalmitoyllecithin. *Biochemistry* 15:4575–4580
- [18] Janiak, M. J., D. M. Small, and G. G. Shipley, 1979. Temperature and compositional dependence of the structure of hydrated dimyristoyl lecithin. *J. Biol. Chem.* 254:6068–6078
- [19] Kaasgaard, T., C. Leidy, J. H. Crowe, O. G. Mouritsen, and K. Jorgensen, 2003. Temperature-controlled structure and kinetics of ripple phases in one- and two-component supported lipid bilayers. *Biophys. J.* 85:350–360
- [20] Katsaras, J., S. Tristram-Nagle, Y. Liu, R. L. Headrick, E. Fontes, P. C. Mason, and J. F. Nagle, 2000. Clarification of the ripple phase of lecithin bilayers using fully hydrated, aligned samples. *Phys. Rev. E* 61:5668–5677
- [21] Kolb, H.-A., O. Enders, and R. Schauer, 1999. Morphology of native and reconstituted biological membranes and their com-

- ponents analysed with atomic force microscopy. *Appl. Phys. A* 68:247–254
- [22] Koynova, R. and M. Caffrey, 1998. Phases and phase transitions of the phosphatidylcholines. *Biochim. Biophys. Acta* 1376:91–145
- [23] Kucerka, N., M. A. Kiselev, and P. Balgavy, 2003. Determination of bilayer thickness and lipid surface area in unilamellar dimyristoylphosphatidylcholine vesicles from small-angle neutron scattering curves: A comparison of evaluation methods. *Eur. Biophys. J.* e-print, DOI: 10.1007/s00249-003-0349-0
- [24] Leidy, C., T. Kaasgaard, J. H. Crowe, O. G. Mouritsen, and K. Jorgensen, 2002. Ripples and the formation of anisotropic lipid domains: Imaging two component supported double bilayers by atomic force microscopy. *Biophys. J.* 83:2625–2633
- [25] LÖbbecke, L. and G. Ceve, 1995. Effects of short-chain alcohols on the phase behaviour and interdigitation of phosphatidylcholine bilayer membranes. *Biochim. Biophys. Acta* 1237:59–69
- [26] Mabrey, S., P. L. Mateo, and J. M. Sturtevant, 1978. Ca^{2+} binding to phosphatidylcholine bilayers as studied by deuterium magnetic resonance. Evidence for the formation of a Ca^{2+} complex with two phospholipid molecules. *Biochemistry* 17:2464–2468
- [27] Mabrey, S. and J. M. Sturtevant, 1976. Investigation of phase transitions of lipids and lipid mixtures by sensitivity differential scanning calorimetry. *Proc. Natl Acad. Sci. USA* 73:3862–3866

-
- [28] Mattai, J., P. K. Sripada, and G. G. Shipley, 1987. Mixed-chain phosphatidylcholine bilayers: Structure and properties. *Biochemistry* 26:3287–3297
- [29] Matuoka, S., S. Kato, M. Akiyama, Y. Amemiya, and I. Hatta, 1990. Temperature dependence of the ripple structure in dimyristoylphosphatidylcholine studied by synchrotron X-ray small-angle diffraction. *Biochim. Biophys. Acta* 1028:103–109
- [30] Matuoka, S., S. Kato, and I. Hatta, 1994. Temperature change of the ripple structure in fully hydrated dimyristoylphosphatidylcholine/cholesterol multibilayers. *Biophys. J.* 67:728–736
- [31] Matuoka, S., H. Yao, S. Kato, and I. Hatta, 1993. Condition for the appearance of the metastable $P_{\beta'}$ phase in fully hydrated phosphatidylcholines as studied by small-angle x-ray diffraction. *Biophys. J.* 64:1456–1460
- [32] McIntosh, T. J., S. A. Simon, and R. C. MacDonald, 1980. The organization of n-alkanes in lipid bilayers. *Biochim. Biophys. Acta* 597:445–463
- [33] Meyer, H. W., 1996. Pretransition-ripples in bilayers of dipalmitoylphosphatidylcholine: Undulation or periodic segments? A freeze-fracture study. *BBA-Lipid Lipid Met.* 1302:138–144
- [34] Meyer, H. W., B. Dobnerb, and K. Semmler, 1996. Macroripple-structures induced by different branched-chain phosphatidylcholines in bilayers of dipalmitoylphosphatidylcholine. *Chem. Phys. Lipids* 82:179–189

-
- [35] Mortensen, K., W. Pfeiffer, E. Sackmann, and W. Knoll, 1988. Structural properties of a phosphatidylcholine-cholesterol system as studied by small-angle neutron scattering: Ripple structure and phase diagram. *Biochim. Biophys. Acta* 945:221–245
- [36] Mou, J., J. Yang, C. Huang, and Z. Shao, 1994. Alcohol induces interdigitated domains in unilamellar phosphatidylcholine bilayers. *Biochemistry* 33:9981–9985
- [37] Mou, J., J. Yang, and Z. Shao, 1994. TRIS (hydroxymethyl)aminomethane ($C_4H_{11}NO_3$) induced a ripple phase in supported unilamellar phospholipid bilayers. *Biochemistry* 33:4439–4443
- [38] Nagano, H., T. Nakanishi, H. Yao, and K. Ema, 1995. Effect of vesicle size on the heat capacity anomaly at the gel to liquid-crystalline phase transition in unilamellar vesicles of dimyristoylphosphatidylcholine. *Phys. Rev. E* 52:4244–4250
- [39] Naghibi, H., A. Tamura, and J. M. Sturtevant, 1995. Significant discrepancies between van't Hoff and calorimetric enthalpies. *Proc. Natl Acad. Sci. USA* 92:5597–5599
- [40] Nagle, J. F. and S. Tristram-Nagle, 2000. Structure of lipid bilayers. *Biochim. Biophys. Acta* 1469:159–195
- [41] Rowe, E. S. and J. M. Campion, 1994. Alcohol induction of interdigitation in distearoylphosphatidylcholine: Fluorescence studies of alcohol chain length requirements. *Biophys. J.* 67:1888–1895
- [42] R uppel, D. and E. Sackmann, 1983. On defects in different phases of two-dimensional lipid bilayers. *J. Phys.-France* 44:1025–1034

-
- [43] Seelig, J., 1990. Interaction of phospholipids with Ca^{2+} ions. On the role of the phospholipid head groups. *Cell Biol. Int. Rep.* 14:353–360
- [44] Sengupta, K., V. A. Raghunathan, and J. Katsaras, 1999. Structure of the ripple phase in chiral and racemic dimyristoylphosphatidylcholine multibilayers. *Phys. Rev. E* 59:2455–2457
- [45] Sengupta, K., V. A. Raghunathan, and J. Katsaras, 2003. Structure of the ripple phase of phospholipid multibilayers. *Phys. Rev. E* 68:031710/1–12
- [46] Shen, Y.-M. A., O. I. Chertihin, R. L. Biltonen, and J. J. Sando, 1999. Lipid-dependent activation of protein kinase C- α by normal alcohols. *J. Biol. Chem.* 274:34036–34044
- [47] Somogyi, R. and H.-A. Kolb, 1988. Cell-to-cell channel conductance during loss of gap junctional coupling in pairs of pancreatic acinar and chinese hamster ovary cells. *Pflugers Arch.* 412:54–65
- [48] Stamatoff, J., B. Feuer, H. J. Guggenheim, G. Tellez, and T. Yamane, 1982. Amplitude of rippling in the P beta phase of dipalmitoylphosphatidylcholine bilayers. *Biophys. J.* 38:217–226
- [49] Sturtevant, J. M., 1998. The effect of sodium chloride and calcium chloride on the main phase transition of dimyristoylphosphatidylcholine. *Chem. Phys. Lipids* 95:163–168
- [50] Sun, W.-J., S. Tristram-Nagle, R. M. Suter, and J. H. Nagle, 1996. Structure of the ripple phase in lecithin bilayers. *Proc. Natl Acad. Sci. USA* 93:7008–7012

-
- [51] Takens-Kwak, B. R., H. J. Jongasma, M. B. Rook, and A. C. V. Ginneken, 1992. Mechanism of heptanol-induced uncoupling of cardiac gap junctions: a perforated patch-clamp study. *Am. J. Physiol.* 262:C1531–C1538
- [52] Tardieu, A., V. Luzzati, and F. C. Remann, 1973. Structure and polymorphism of the hydrocarbon chains of lipids. *J. Mol. Biol.* 75:711–733
- [53] Tokumasu, F., A. J. Jin, and J. Dvorak, 2002. Lipid membrane phase behaviour elucidated in real time by controlled environment atomic force microscopy. *Journal of Electron Microscopy* 51:1–9
- [54] Valiyaveetil, F., Y. Zhou, and R. MacKinnon, 2002. Lipids in the structure, folding, and function of the KcsA K⁺ channel. *Biochemistry* 41:10771–10777
- [55] Verkleij, A. J., P. H. Ververgaert, L. L. van Deenen, and P. F. Elbers, 1972. Phase transitions of phospholipid bilayers and membranes of *Acholeplasma laidlawii* B visualized by freeze fracturing electron microscopy. *Biochim. Biophys. Acta* 288:326–332
- [56] Wack, D. C. and W. W. Webb, 1989. Synchrotron x-ray study of the modulated lamellar phase P_{β}' in the lecithin water system. *Phys. Rev. A* 40:2712–2730
- [57] Williamson, I. M., S. J. Alvis, J. M. East, and A. G. Lee, 2003. The potassium channel KcsA and its interaction with the lipid bilayer. *Cell. Mol. Life Sci.* 60:1581–1590

-
- [58] Woodward, J. T. and J. A. Zasadzinski, 1996. Amplitude, wave form and temperature dependence of bilayer ripples in the $P_{\beta'}$ phase. *Phys. Rev. E* 53:R3044–R3050

8 Lorentz-force-induced Excitation of Cantilevers for Oscillation-Mode Scanning Probe Microscopy

O. Enders^α, F. Korte^γ and H.-A. Kolb^α

^α Institute of Biophysics, University Hannover, Herrenhäuser Str. 2, D-30419 Hannover, Germany

^γ Laser Zentrum Hannover e.V., Hollerithallee 8, D-30419 Hannover, Germany

Surface and Interface Analysis, vol. 36, 2004, p. 119-23

Copyright John Wiley & Sons Limited. Reproduced with permission.

Abstract

In the field of scanning probe microscopy, imaging modes with oscillating cantilevers are used to image soft samples with high resolution. The tapping mode is most frequently realized by a vibrating chip-holder which is coupled to the cantilever-chip to excite the cantilever acoustically. A new promising approach is a direct excitation of a V-shaped cantilever by a Lorentz force acting on a V-shaped cantilever. The Lorentz force is generated by an alternating current flowing through the cantilever while being placed in a static magnetic field. Here we show an appropriate method to micro-structure the reflective coating of commercial cantilever-chips for a current flow through the cantilever, which is based on a laser system. The laser micro-structuring method allows to process the chips without changing the mechanical properties of the cantilever itself, leading to excellent dynamic properties of the vibrating cantilever. Since the cantilever is excited directly, no peripheral resonances except the eigenresonance of the cantilever were apparent in the frequency spectrum. For a current of high amplitude at a static magnetic field of low intensity it is observed that the bi-metal properties of the cantilever cause an additional thermal excitation. The results show that commercial cantilevers can be micro-structured to implement this new excitation method for a frequency spectrum with a high quality factor of oscillation.

8.1 Introduction

The atomic force microscope [1] has been used in many fields of applied and natural science to elucidate the topography and physical

properties of surfaces and molecules with a resolution up to atomic level [5]. An important improvement was the development of an oscillating cantilever mode (AC-mode), which allows to image soft sample surfaces with less shear distortion [12]. At first real non-contact modes were performed, using piezo excited cantilevers. In this mode the cantilever and the tip oscillate at a distance of a few angstrom above the sample surface. But in fluids non-contact measurements were not applicable, since this mode requires a high quality factor of oscillation, which is reduced to values in the order of one by hydrodynamic damping [15]. The first AC-mode which was successfully applied to image samples in fluids was the so called tapping mode [7, 13]. For this mode the vibrating fluid cell excites the cantilever acoustically. The image contrast is determined by the oscillation amplitude of the cantilever which is damped by periodically contacting the sample. The tapping mode was successfully applied to image soft biological samples with high resolution. The broad spectrum of samples ranges from adsorbed DNA-molecules [7] and membrane proteins [17] to the dynamic analysis of growing protein crystals in their crystallizing solution [18]. However, for this mode the cantilever is not excited directly, but by oscillations of the surrounding fluid cell, which couples to the adjacent fluid, the sample and finally to the cantilever-chip. As a consequence the frequency spectrum of the excited cantilever is superimposed by peaks mainly caused by resonances of the fluid cell [7, 15]. The frequency spectrum could be improved by invention of the magnetic AC mode (m.a.c.-mode) [6]. In this mode the cantilever-chip is coated with a ferromagnetic material and excited by an alternating magnetic field. This mode could successfully be applied in molecular recognition force microscopy [16]. However, in the m.a.c.-mode not only the cantilever is excited, but also the chip. Thus the resonance spectrum

of the cantilever is still distorted by resonances, which are probably caused by oscillations of the cantilever chip.

Recently a new excitation method was reported, which is based on the Lorentz force acting on an alternating current flowing through a V-shaped cantilever, which is placed into a static magnetic field, at appropriate orientation and strength [2]. However this approach requires a costly post processing step of the cantilever sensors, which limits the general use of the method.

In this paper we present a simple and efficient implementation of Lorentz force induced excitation of cantilevers. Commercial cantilever can be used. The post processing step is performed by a laser based micro-structuring unit. The excitation method can be easily installed in commercial force microscopes, and requires only commercial cantilevers, which are supplied with a thin conducting reflection layer. The magnetic excitation affects the cantilever only, which responds as a driven damped harmonic oscillator in air as well as in fluid.

8.2 Material and methods

8.2.1 Basic setup

The excitation by Lorentz force depends on an alternating current through a V-shaped cantilever (CSC 21, Anfattec, Dresden) interacting with an external static magnetic field. Since most commercially available cantilevers have a reflective Al- or Au- coating on their backside and an insulating substrate, this coating was used as conductor. To achieve a current flow through the V-shaped cantilever, the reflective layer is disrupted in a way, so that both ends of the V-shaped cantilever become electrically insulated (see fig. 8.1). The voltage was

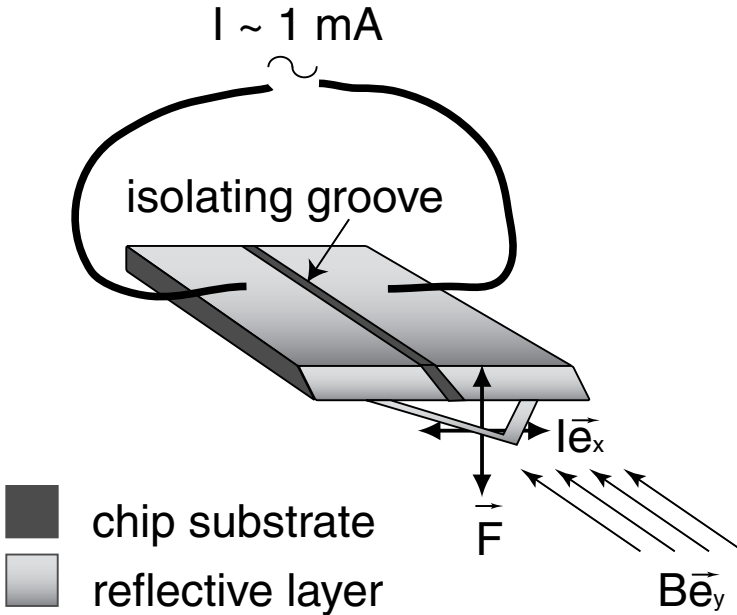


Figure 8.1: Schematic setup for Lorentz force excitation of the cantilever. The reflective layer of the chip was disrupted by a laser based micro-structuring unit. The two remaining layers on the chip are electrically connected by the reflective layer on the backside of the cantilever only. A sinusoidal current (I) is applied to the micro-structured reflective layer of the chip. Assuming that the magnetic field strength has a sufficient large component in direction of \vec{e}_y , and a sinusoidal current is flowing through the cantilever, the cantilever is deflected periodically in vertical direction. \vec{F} denotes the Lorentz force; \vec{B}_y , the static magnetic field and $I\vec{e}_x$ the effective current through the cantilever.

applied by an enameled winding wire of copper (Conrad Elektronik, Germany), which was directly connected to the two separated parts of the reflective and conductive layer on the chip surface. The wire was fixed by an electrically conductive two component epoxy glue (Circuit Works, Chemtronics Kennesaw, USA).

In order to generate an oscillating torque which drives the cantilever, a magnetic field is applied. The important requirement is a sufficient large component of the magnetic field, which is oriented perpendicular to the magnetic moment of the cantilever as well as to its bending axis. In contrast to other magnetic AC-modes, the required magnetic field is static. For application of a static magnetic field cylindrical NdFeB-permanent magnets (Beloh, Hameln, Germany) were used, which were magnetized along their cylindric axis.

In order to characterize the system for measurements in air a commercial setup was used. The permanent magnets were properly placed close to the cantilever. The set up consists of the basic components of a modified scanning force microscope (Multimode, Nanoscope IIIa, Veeco Instruments, Santa Barbara, USA). For the analysis of the frequency spectrum of the cantilever the scanning unit was omitted. The signal generation and acquisition was performed by a LabView system equipped with a MIO E 16-4 data acquisition card (National Instruments) at a sample rate of 400 kSamples/s. The dynamic properties of the oscillation were evaluated by tuning the frequency of the sinusoidal current above and below the eigenfrequency of the cantilever. For each frequency, the real time deflection data were acquired. These data were band pass filtered to remove low frequency noise. Afterwards the signal-power was calculated and saved.

For fluid measurements in fluids, the set up was supplemented by a fluid cell (Veeco Instruments, Santa Barbara, USA). The LabView-

system described above, was connected between the microscope and the controller. The permanent magnets were placed above the fluid cell, which contained the micro-structured cantilever chip. The fluid cell was filled with distilled water.

8.2.2 Micro-structuring the cantilever chip

The most critical step during the preparation of the Lorentz force induced excitation concerned the micro-structuring of the cantilever chip. We applied a laser-based ablation method [9], to cut a groove into the reflective layer of the chip, as schematically shown in fig. 8.1. For micro-structuring a femtosecond pulse laser combined with a 2D galvo scanning head was used. The femtosecond laser pulses were generated by a commercial Titan:Sapphire laser (Spitfire, Spectra Physics, Inc.). The wavelength was 780 nm at a pulse duration of 130 fs. The laser beam was focused by an achromate of 100 mm focal length. A pulse energy of 10 μJ at a repetition rate of 1 kHz, and a feed rate of 1 mm/s were used in order to adjust the groove depth sufficiently to remove the reflective layer. After the chips were mounted on a cover slip, the laser scanning unit was programmed to cut the required line with μ -accuracy. The obtained groove width was about 30 μm . With this method about ten cantilever chips could be processed in less a minute. After processing, the debris was removed by washing in distilled water. Since the width of the groove can be reduced to the wavelength of the laser system, also chips, which carry V-shaped cantilevers having a small separation between the two connections to the chip, may be processed by this method.

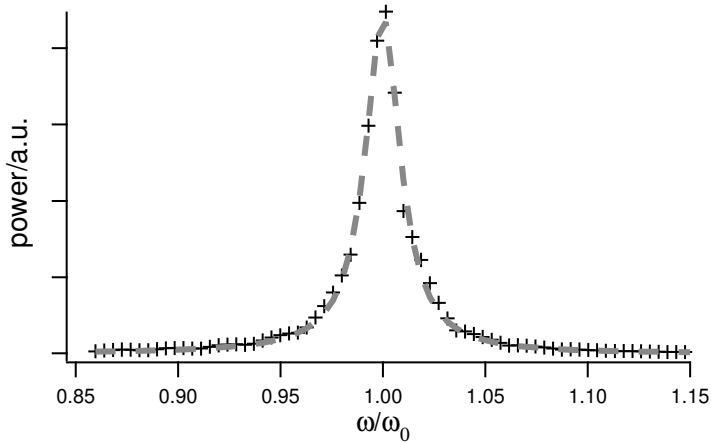


Figure 8.2: Power spectrum of a Lorentz force excited cantilever in air (crosses). The bandwidth limited mean signal-power of the deflection is given in arbitrary units (a.u.) as function of the normalized angular excitation frequency ω . The measured eigenfrequency of the cantilever was about $\frac{\omega_0}{2\pi} = 14$ kHz. The presented curve was measured using six strong permanent magnets (see 8.2.1) placed in close proximity of the cantilever. The dashed curve represents the fit of equation (8.1) for a damped harmonic oscillator. The peak-to-peak amplitude of the AC-current through the V-shaped cantilever was 0.5 mA.

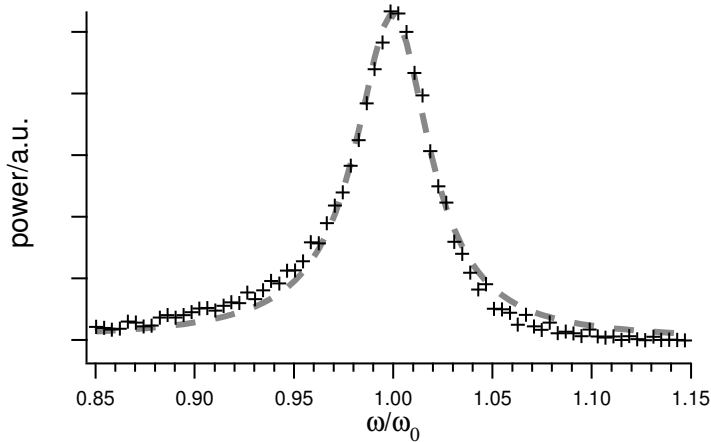


Figure 8.3: Power spectrum of a Lorentz force excited cantilever placed in a water containing fluid cell (crosses). The bandwidth limited mean signal-power of the deflection is given in arbitrary units as function of angular excitation frequency ω . The measured eigenfrequency of the cantilever was about $\frac{\omega_0}{2\pi} = 25$ kHz. Six permanent magnets are placed about 5 mm above the cantilever. The excitation AC-current was adjusted to about 1.5 mA (peak-to-peak). The power spectrum was fitted by equation (8.1)

8.3 Results

For the experiments, cantilevers with two different geometric and dynamic properties were prepared. For measurements in ambient air, a soft cantilever with a nominal spring constant of 0.03 N/m and a resonance frequency at nominal 14 kHz was used. This frequency matches the limited bandwidth of the signal acquisition hardware. For the measurements in fluids cantilevers with higher resonance frequency of nominal 105 kHz and force constant of nominal 0.6 N/m could be used. The micro-structured cantilever chips had an electrical resistance in the range of 50 Ω to 150 Ω . The applied voltage was adjusted by an appropriate resistor in series, to obtain a peak-to-peak AC-current of about 0.5 mA through the cantilever. Assuming a two dimensional conducting loop as model of the magnetic behavior of the cantilever, a magnetic moment of about 5×10^{-12} Am² for the stiff cantilever and about $50 \cdot 10^{-12}$ Am² for the soft cantilever could be calculated. In order to obtain a Lorentz force of about 0.1 nN a magnetic field strength of about 2 mT or about 0.5 mT has to be applied, respectively. These values can be easily achieved by use of commercial permanent magnets, if they are placed sufficiently close to the cantilever.

The power spectrum, which is shown in fig. 8.2, was acquired in ambient air using the setup described in 8.2.1. The amplitude of the power spectrum A^2 was normalized and is given as function of the ratio of angular frequency (ω) of the AC-current and the eigenfrequency of the cantilever (ω_0). Similar to the results of [6], the power spectrum consists of only one resonance peak and shows a shape known for the

driven damped harmonic oscillator. The latter can be described as follows [14]

$$A^2(\omega) = a^2 \frac{Q^2}{Q^2 \left(1 - \frac{\omega^2}{\omega_0^2}\right)^2 + \frac{\omega^2}{\omega_0^2}} \quad (8.1)$$

where ω_0 is the resonant angular frequency, $a \cdot Q$ is the resonant amplitude, ω is excitation angular frequency, Q is quality factor of the oscillator and $A(\omega)^2$ the power spectrum. The best fit of equation (8.1) to the spectrum in fig. 8.2 revealed a Q value of about 50.

For the measurements at fluid conditions, a cantilever of smaller spring constant (0.6 N/m) was mounted to a commercial scanning force microscope which was equipped with a fluid cell (see 8.2.1). Although the minimum distance of the cantilever to the permanent magnets was about 5 mm the cantilever could be excited to oscillations. To be sure that oscillation were not caused by thermal excitation, the magnets were removed and a decline of the signal amplitude was observed. This decline indicates, that the excitation is caused by Lorentz force. The measured frequency spectrum is shown in fig. 8.3.

Similar to the results of [13], [15] and [3] a remarkable decrease of the apparent eigenfrequency occurred. In the spectrum shown in fig. 8.3 an apparent resonance frequency of 24.9 kHz was measured, which is about 3 to 5 times smaller than the nominal eigenfrequency of this type of cantilever. This effect cannot be simply explained by the lower quality factor in fluids compared to the experiments in ambient air. The decrease of resonance frequency can be interpreted by an effective increase in mass [3, 4]. This increase can be modeled by an hydrodynamic drag depending on acceleration [10].

In contrast to the m.a.c.-mode introduced by [6] no further peripheral resonance peaks are visible in the spectrum (fig. 8.3). The mea-

sured power spectrum can be reasonably well described by a damped harmonic oscillator. A non-significant deviation of the fitted curve to the measured data can be seen at raising and falling edge of the resonance peak. The absence of further resonance frequencies indicates, that the cantilever is excited directly. The oscillating force, which acts on the chip, can be neglected in a first approximation. This arises from the fact, that the force acting on the chip is of the same order of magnitude compared to the force which excites the cantilever. But in the conventional m.a.c.-mode, the force acting on the chip can be expected to be several magnitudes larger than for the cantilever. This finding could be caused by an increase of the magnetic force with the amount of magnetic material [6]. For a chip the coated area is several magnitudes larger than on the backside of the cantilever. Therefore, it can be expected that the chip and the adjacent fluid is excited stronger compared to Lorentz-excitation.

The quality factor, which can be derived from fig. 8.3 is about 20. This value is in the upper range of quality factors generally observed for cantilevers immersed in fluids. The fact, that the cantilever surface is not significantly altered by the laser micro-structuring process of the chip has the advantage, that the corresponding mechanical properties like mass, force constant and eigenfrequency of the cantilever remain about unchanged.

However, if the peak to peak current is increased to about 10 mA while the external magnetic field is reduced by removing some of the permanent magnets, a second peak appears in the amplitude spectrum of the vibrating cantilever at an angular frequency two times the excitation angular frequency (ω_1 , in fig. 8.4 a.). This behavior is only observed if the cantilever is immersed into water. In contrast to excitation of higher harmonics [2, 4], the cantilever does not only respond

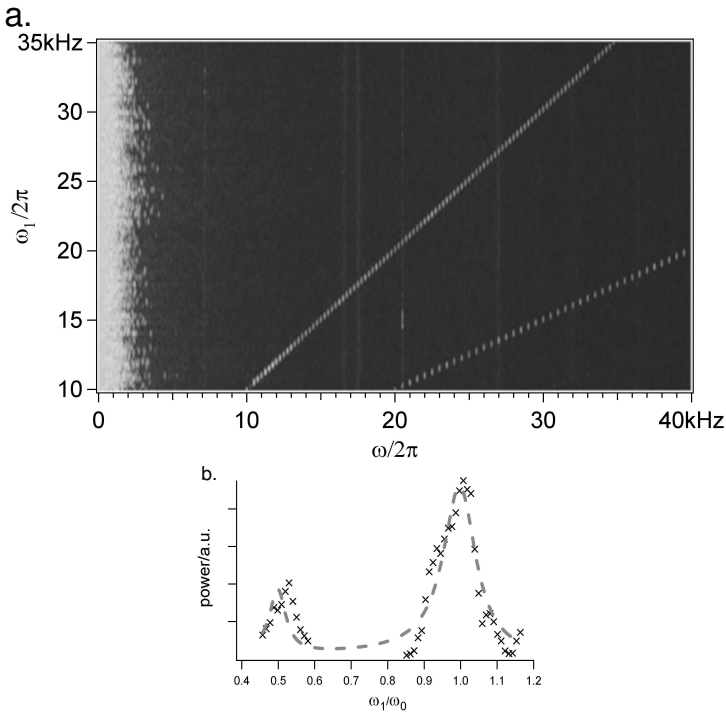


Figure 8.4: Amplitude spectrum and power spectrum of cantilever oscillation which is excited by Lorentz force superimposed by a thermal induced oscillation at low magnetic field and high electrical current (about 10 mA) in water. Image a. shows the Fourier transformed deflection signal (color coded: light colors correspond to a high, dark colors to a low amplitude) in dependence on the excitation frequency $\omega_1/2\pi$ (y-axis) and the independent variable $\omega/2\pi$ (x-axis). Light spots correspond to high amplitude oscillations. The cantilever oscillates with the frequency of the excitation current and twice of it. Image b. shows a power spectrum at similar conditions. The signal power was recorded while the frequency of the excitation current was shifted around the cantilever resonance frequency as well as around half of this value (crosses). The dashed curve represents a fit of equation (A8.12) to the experimental data, which was derived from a model of cantilever oscillations, which includes thermal excitation by power dissipation. The latter is caused by the alternating current through the cantilever.

to the excitation angular frequency ω_1 but also to $2\omega_1$. This effect can only arise if the excitation current leads to an additional force on the cantilever which cannot be explained by Lorentz force. A possible explanation for this additional force could be a periodic bending of the cantilever, which is caused by a rapid heating by the electrical power and subsequent fast dissipation by the adjacent fluid. Similar effects were reported by [8]. This process occurs at two times the excitation frequency, because the heating power is proportional to the squared amplitude of the excitation current. Focusing on the spectrum of the signal power in dependence on the excitation frequency (fig. 8.4 b.), it can be expected that an additional apparent resonance peak emerges, at a frequency 0.5 times the true resonance of the cantilever. As shown in the appendix, a corresponding power spectrum can be modeled analytically. In order to prove the model, the power spectrum of the cantilever was recorded in a frequency range including the true resonance and frequencies around round half of this value (fig. 8.4 b.). A fit of the function $P(\omega_N)$ (equation (A8.12), appendix) could be performed. Beside some small deviations which may be caused by the filter properties of the electronics of the photo-diode stage of the scanning force microscope, the function described by equation (A8.12) agrees suitable with the experimental data.

In spite of the fact, that these thermal effects could disturb measurements, they can be reduced to a negligible level by using a sufficient strong magnetic field, which allows low excitation currents. However, the thermal effect could be used as an additional excitation scheme, if an appropriate static magnetic field cannot be established.

8.4 Conclusion

In this paper we present an implementation of a new electromagnetic excitation method for scanning probe microscopes operating with oscillating cantilevers. In contrast to a known implementation, commercial cantilevers were micro-structured by a laser based method. The measured power spectra can be suitably fitted by the model of a single driven damped harmonic oscillator without peripheral resonances in air and fluid. This indicates, that the cantilever is directly excited without significant forces acting on peripheral parts like the cantilever chip or the chip holder. However if the external magnetic field is reduced and the excitation current significantly increased, the cantilever can be excited by thermal oscillations of the bi-metal like cantilever. This leads to an apparent resonance peak at half the frequency of the excitation current in fluids. Since the cantilevers can be processed with low expenses by the laser based micro-structuring, the new excitation method can be easily implemented into scanning force microscopes. Besides an implementation of this new excitation mode in scanning probe microscopes a wider field of application is conceivable. This may include sensor arrangements, which are based on micro-mechanical oscillating cantilevers and tuning fork techniques [11].

Appendix

8.4.1 Thermal and Lorentz force induced excitation

The cantilever oscillation is described as damped harmonic oscillation according to

$$(\partial_t^2 + \frac{\omega_0}{Q}\partial_t + \omega_0^2)z(t) = f(t) \quad (\text{A8.2})$$

$z(t)$ is the z-Position of the cantilever, Q is quality factor of the free oscillation and ω_0 is angular velocity at resonance. The driving force is given by

$$f(t) = a \cdot \cos(\omega_1 t) + b \cdot \cos^2(\omega_1 t) - \frac{b}{2} \quad (\text{A8.3})$$

The first term reflects the contribution due to the Lorentz force induced by the oscillating current. The middle term reflects the bending force due to periodic heating and cooling of the bi-metal like cantilever. This term is assumed to be proportional to the signal power of the excitation current ($I(t) = I_0 \cdot \cos(\omega_1 t)$). The last term takes into account that the mean of $f(t)$ should be zero. A possible phase difference between both contributions is neglected. Introducing the dimension-free time $x = \omega_0 \cdot t$ and using the spring constant κ equations (A8.2) and (A8.3) can be written as

$$\kappa(\partial_x^2 + \frac{1}{Q}\partial_x + 1)y(x) = r(x) \quad (\text{A8.4})$$

where

$$r(x) = a \cdot \cos(\omega_N \cdot x) + b \cdot \cos^2(\omega_N \cdot x) - \frac{b}{2} \quad (\text{A8.5})$$

and $\omega_N = \frac{\omega_1}{\omega_0}$. Assuming that at $t = -\infty$ the z-Position and velocity of the cantilever is zero, the corresponding Green-function of the oscillator is:

$$\tilde{g}(k) = \frac{Q}{\kappa} \frac{1}{Q - k^2 Q + ik} \quad (\text{A8.6})$$

and the Fourier transformed $\tilde{r}(k)$ of $r(x)$ becomes

$$\begin{aligned} \tilde{r}(k) = & \frac{\pi}{2} (2a \cdot (\delta(k + \omega_N) + \delta(k - \omega_N)) + \\ & + b \cdot (\delta(k + 2\omega_N) + \delta(k - 2\omega_N))) \end{aligned} \quad (\text{A8.7})$$

The Fourier transformed of $y(t)$ is

$$\tilde{y}(k) = \tilde{g}(k) \cdot \tilde{r}(k) \quad (\text{A8.8})$$

$$= \frac{\pi Q}{2\kappa} \left(\frac{2a(\delta(k + \omega_N) + \delta(k - \omega_N))}{Q - k^2 Q + ik} + \right. \quad (\text{A8.9})$$

$$\left. + \frac{b(\delta(k + 2\omega_N) + \delta(k - 2\omega_N))}{Q - k^2 Q + ik} \right) \quad (\text{A8.10})$$

The signal power can be written in the frequency domain as

$$P(\omega_N) = \frac{1}{2\pi} \int dk |\tilde{y}(k)|^2 \quad (\text{A8.11})$$

which is solved as

$$\begin{aligned} P(\omega_N) = & \frac{\pi Q^2}{\kappa^2} \left(\frac{a^2}{\omega_N^4 Q^2 - 2\omega_N^2 Q^2 + Q^2 + \omega_N^2} + \right. \\ & \left. + \frac{b^2}{4(16\omega_N^4 Q^2 - 8\omega_N^2 - 8\omega_N^2 Q^2 + Q^2 + 4\omega_N^2)} \right) \end{aligned} \quad (\text{A8.12})$$

Equation (A8.12) can be used to describe the observed signal-power as function of excitation frequency.

References

- [1] Binnig, G., C. Quate, and C. Gerber, 1986. Atomic force microscope. *Phys. Rev. Lett.* 56:930
- [2] Buguin, A., O. D. Roure, and P. Silberzan, 2001. Active atomic force microscopy cantilevers for imaging in liquids. *Appl. Phys. Lett.* 78:2982–2984
- [3] Butt, H. J., P. Siedle, K. Seifert, K. Fendler, T. Seeger, E. Bamberg, A. I. Weisenhorn, K. Goldie, and A. Engel, 1995. Scan speed limit in atomic force microscopy. *J. Microsc.* 169 Pt. 1:75–84
- [4] Chen, G. J., R. J. Warmack, T. Thundat, D. P. Allison, and A. Huang, 1994. Resonance response of scanning force microscopy cantilevers. *Rev. Sci. Instrum.* 65:2532–2537
- [5] Giessibl, F. J., S. Hembacher, H. Bielefeldt, and J. Mannhart, 2000. Subatomic features on the silicon (111)-(7x7) surface observed by atomic force microscopy. *Science* 289:422–425
- [6] Han, W., S. M. Lindsay, and T. Jing, 1996. A magnetically driven oscillating probe microscope for operation in liquids. *Appl. Phys. Lett.* 69:4111–4113
- [7] Hansma, P. K., J. P. Cleveland, M. Radmacher, D. A. Walters, P. E. Hillner, M. Bezanilla, M. Fritz, D. Vie, H. G. Hansma, C. B.

- Prater, J. Massie, L. Fukunaga, J. Gurley, and V. Elings, 1994. Tapping mode atomic-force microscopy in liquids. *J. Appl. Phys.* 64:1738–1740
- [8] Hillier, A. C. and A. J. Bard, 1997. ac-mode atomic force microscope imaging in air and solutions with a thermally driven bimetallic cantilever probe. *Rev. Sci. Instrum.* 68:2082–2090
- [9] Korte, F., S. Nolte, B. Chichkov, T. Bauer, G. Kamlage, T. Wagner, C. Fallnich, and H.-A. Welling, 1999. Far-field and near-field material processing with femtosecond laser pulses. *Appl. Phys. A* 69:7–11
- [10] Landau, L. D. and E. M. Lifshitz, 1959. Fluid Mechanics. Pergamon, New York
- [11] Lang, H. P., R. Berger, F. Battiston, J.-P. Ramseyer, E. M. C. Andreoli, J. Brugger, P. Vettiger, M. Despont, T. Mezzacasa, L. Scandella, H. J. Güntherodt, C. Gerber, and J. K. Gimzewski, 1998. A chemical sensor based on a micromechanical cantilever array for the identification of gases and vapors. *Appl. Phys. A.* 66:S61–64
- [12] Martin, Y., C. C. Williams, and H. K. Wickramasinghe, 1987. Atomic force microscope force mapping and profiling on a sub 100-Å scale. *J. Appl. Phys.* 61:4723–4729
- [13] Putman, C. A. J., K. O. V. der Werf, B. G. D. Grooth, N. F. van Hulst, and J. Greve, 1994. Tapping mode atomic force microscopy in liquid. *Appl. Phys. Lett.* 64:2454–2456

-
- [14] Sarid, D., 1994. Scanning Force Microscopy, chapter 2.4. Oxford Univ. Press, New York
- [15] Schäffer, T. E., J. P. Cleveland, F. Ohnesorge, D. A. Walters, and P. K. Hansma, 1996. Studies of vibrating atomic force microscope cantilevers in liquid. *J. Appl. Phys.* 80:3622–3627
- [16] Schindler, H., D. Badt, P. Hinterdorfer, F. Kienberger, A. Raab, S. Wielert-Badt, and V. P. Pastuschenko, 2000. Optimal sensitivity for molecular recognition MAC-mode AFM. *Ultramicroscopy* 82:227–235
- [17] Stark, M., C. Möller, D. J. Müller, and R. Guckenberger, 2001. From images to interactions: High-resolution phase imaging in tapping-mode atomic force microscopy. *Biophys. J.* 80:3009–3018
- [18] Wichmann, M., O. Enders, C. Zeilinger, and H. A. Kolb, 2001. Analysis of protein crystal growth at molecular resolution by atomic force microscopy. *Ultramicroscopy* 86:159–166

Acknowledgment

My appreciation and thanks for the accomplishment of the thesis is directed to Prof. Dr. H.-A. Kolb for giving me the opportunity to work in his group and for the years of support and scientific discussion. His mentoring has synthesized the freedom for following own ideas and creativity and the guidance to focus on the final aim.

The effort of my external examiner Prof. Dr. W. Ertmer for the evaluation of the dissertation is highly acknowledged.

For the patience to explain the art of isolating vacuoles from barley to a double left-handed physicist, I thank Prof. Dr. E. Martinoia.

For the effort of providing me with gap-junctions and protocols I would like to show appreciation to Dr. O. Traub and Dr. M. Yeager. Furthermore I would like to mention Prof. Dr. E. Gulbins for the fruitful cooperation and the ceaseless sending of lipid rafts.

I thank Dr. F. Korte for the friendly and prolific cooperation and I wish him good luck and all the best for the formation of his company and family.

Dr. A. Ngezahayo and Dr. C. Zeilinger have ceaselessly tried to teach me the biological background story, thank you.

I am grateful for the always backing and friendly cooperation of my colleagues at our AFM-group, M. Wiechmann, R. Schauer and F. Leisten and the technical support of H. Bliedung, I. Buchwald as well as for the excellent workings of R. Groffmann, H. G. Hannibal, F. Koepke and M. Senft.

Special thanks are dedicated to all my colleagues and friends at the Institute of Biophysics. It would not have been possible to stand the see-saw of the doctorate's labour without their unselfish support and the generation of the excellent atmosphere (Prof. Dr. A. Anders, B. Altmann, H. Bliedung, Dr. med. A. Blödow, I. Buchwald, Dr. rer. nat. M. Debarry, H. Hake, Dr. rer. nat. J. Hellmer, Dr. med. R. Junker, R. Krebs, M. Kästner, S. Krüger, A. Lika-Gerbing, F. Leisten, Dr. rer. nat. I. Marten, M. Meinhardt, Dr. rer. nat. A. Ngezahayo, R. Pätzold, T. Reeck, R. Schauer, M. Wiechmann and Dr. C. Zeilinger).

For providing additional financial support I would like to thank Prof. Dr. E. Gulbins and Prof. Dr. A. Ernst.

Foremost I would like to thank my parents and Anja for their unlimited support and love.

Curriculum vitae

Oliver Enders
Schaufelder Str. 31
30167 Hannover

Born on March 27, 1972 in Wildeshausen, Germany

- 11.1999 - to date Doctoral studies at the department of biology,
University of Hannover
- 09.2003 - 10.2003 Scientific assistant at the Institute of Biophysics,
University of Hannover
- 08.2003 Scientific assistant at the Institut für Molekular-
biologie, Universitätsklinikum Essen
- 07.1999 - 07.2003 Scientific assistant at the Institute of Biophysics,
University of Hannover
- 06.1998 - 06.1999 Scholar ship holder of Sonnenfeld-Stiftung at the
Institute of Biophysics, University of Hannover
- 08.1998 Physik-Diplom, University of Hannover
- 09.1994 - 07.1995 Physics and biophysics studies, Oulun Yliopisto,
Finland

10.1991 - 05.98	Diploma studies in physics, University of Hannover
1991	Abitur, Gymnasium Wildeshausen
1988 - 1991	Gymnasium Wildeshausen
1984 - 1988	Realschule Wildeshausen
1982 - 1984	Orientierungsstufe Wildeshausen
1978 - 1982	Grundschule Wildeshausen

24th August 2004